ELSEVIER

International Journal of Solids and Structures 41 (2004) 3461–3490

INTERNATIONAL JOURNAL OF SOLIDS and STRUCTURES

www.elsevier.com/locate/ijsolstr

A multi-scale constitutive formulation for the nonlinear viscoelastic analysis of laminated composite materials and structures

Rami M. Haj-Ali *, Anastasia H. Muliana

School of Civil and Environmental Engineering, Georgia Institute of Technology, 790, Atlanta, GA 30332-0355, USA

Received 17 September 2003; received in revised form 16 January 2004
Available online 12 March 2004

Abstract

This paper presents an integrated micromechanical and structural framework for the nonlinear viscoelastic analysis of laminated composite materials and structures. Each unidirectional lamina is idealized using the Aboudi four-cell micromodel with incremental formulation in terms of the average strain and stress in the subcells. The fiber medium is considered as transversely isotropic and linear elastic. The Schapery nonlinear viscoelastic model is used to describe the isotropic viscoelastic behavior of the matrix subcells. A previously developed recursive–iterative method is employed for the numerical integration of the Schapery model. The subcells' constitutive models are nested through a numerical stress-update algorithm. The latter is based on a predictor–corrector scheme that satisfies the fiber and matrix viscoelastic constitutive relations along with the micromechanical equations in the form of traction continuity and strain compatibility between the subcells. The effect of physical aging on creep is also examined. Several experimental creep tests on off-axis specimen, available in the literature, are used to validate the formulation. The proposed material and structural framework is general and can easily incorporate temperature, moisture, and physical aging effects. The micromechanical model is numerically implemented within a shell-based nonlinear finite element (FE) by imposing a plane stress constraint on its 3D formulation. Examples for nonlinear viscoelastic structural analyses are demonstrated for a laminated panel and a composite ring.

Keyword: Viscoelastic nonlinear micromechanics laminated structures

1. Introduction

Fiber reinforced polymeric (FRP) composites are often used in many modern engineering applications. The effective response of these composites is usually time-dependent due to the existence of polymeric matrix. The matrix viscoelastic behavior depends on its microstructure, previous thermomechanical state, in addition to the current state of loading and environmental conditions. The moisture content can greatly

* Corresponding author. Tel.: +1-404-8944716; fax: +1-404-8940211.
E-mail addresses: rami.haj-ali@ce.gatech.edu, gte573h@prism.gatech.edu (R.M. Haj-Ali).

0020-7683/$ - see front matter © 2004 Elsevier Ltd. All rights reserved.
doi:10.1016/j.ijsolstr.2004.02.008

decrease the energy required to produce deformation at a constant temperature due to the internal reversible changes of the microstructure. In most amorphous polymers, environmental effects such as increasing temperature and moisture content enhance the nonlinear deformation and deterioration of the internal microstructure, especially when coupled with mechanical loading. Nonlinear viscoelastic analysis is considered in the case of large stress levels, especially when combined with elevated temperatures or high moisture conditions. The axial stiffness and strength of unidirectional FRP materials are not usually affected by time-dependent effects, due to the dominant presence of the linear elastic fiber. Nonlinear and time-dependent effects should be considered in the overall FRP constitutive material model in order to achieve efficient designs that meet long-term performance.

Many studies have been performed to test and characterize the linear and nonlinear viscoelastic behaviors of different FRP laminated composites. Off-axis tests have been conducted under different loading levels. The viscoelastic parameters were characterized separately for each off-axis test. Lou and Schapery (1971) performed experimental tests on glass and graphite epoxy composites with different off-axis fiber orientations. Creep response was negligible in the axial (fiber) direction. Pronounced nonlinear viscoelastic behavior was shown in the creep tests for 30° (and higher) off-axis specimens at moderate levels of applied stress. The four nonlinear viscoelastic parameters in the Schapery single integral creep equations were assumed to be functions of the average octahedral shear stress in the matrix. A simplified relation for the matrix octahedral stress was derived as a function of the applied in-plane stresses and the off-axis angle. Yeow et al. (1979) used time–temperature superposition principle (TTSP) to determine the long-term compliances of a unidirectional T300/934 graphite/epoxy composite system. Linear viscoelastic response was shown along the fiber direction, while nonlinear viscoelastic response was shown in the transverse and shear modes. Hiel et al. (1983) used Schapery's nonlinear viscoelastic integral to characterize the long-term viscoelastic behaviors of a T300/934 graphite/epoxy unidirectional composite calibrated from short-term test results. The nonlinear integral relations were calibrated separately for the uniaxial transverse and axial-shear modes. Tuttle and Brinson (1986) conducted creep-recovery test for off-axis T300/5208 graphite/epoxy composites with 0°, 10°, and 90° angles. The viscoelastic parameters in the Schapery model were taken as functions of matrix octahedral stress. The nonlinear viscoelastic model was combined with the classical laminate theory (CLT) to perform nonlinear viscoelastic analysis of graphite–epoxy laminates under in-plane loading. Accelerated method was used based on the time–temperature–stress-superposition principle (TTSSP) in order to predict the long-term creep behavior.

The physical aging of polymers and polymeric composites has been considered. Struik (1978) defined physical aging as the process that a polymeric material undergoes by a gradual continuation of the glass formation below glass transition temperature (T_g). The aging material is not under thermodynamic equilibrium (stable state). This is indicated by a molecular mobility and a slow process to establish equilibrium over time, which cause its mechanical (elastic and viscoelastic) properties change with time. The long-term mechanical behavior of FRP composites in a state below T_g is important for accurate analysis and design of structures. Struik (1978) studied physical aging of various polymers and developed a model to predict long-term viscoelastic behavior based on short-term test data. The momentary master curves (MMC) were created for the short-term test data at various aging times. The effective time was developed to shift the short-term test data using the aging shift factor in order to predict the long-term response. Brinson and Gates (1995) used Struik physical aging theory to model the long-term responses of unidirectional lamina with different off-axis angles. Their model was then used with the CLT to predict the long-term responses of laminated composites. This study indicates a different rate of change in the shear and transverse modes of viscoelastic response due to aging. Gates et al. (1997) studied the effects of physical aging on creep compliances of IM7/K3B composite under tension and compression. Short-term creep tests (96 h) at various temperatures and aging times were performed for laminates with $[90]_{12}$ and $[\pm 45]_{2s}$ layup to determine the transverse and shear responses. The long-term predictions (1500 h) compared well with the experimental data. Pasricha et al. (1997) used the Schapery model with reduced effective time and recursive formulation

to account for the effects of physical aging in laminated composites. The Schapery integral was separately applied for shear and transverse modes. Bradshaw and Brinson (1999a) presented a method to determine the physical aging properties from repeated creep relaxation tests under different isothermal conditions. The effective time theory was employed in the Schapery's hereditary integral equation. Bradshaw and Brinson (1999b) predicted the mechanical response of laminated composites due to physical aging by incorporating their model with the CLT. Each lamina was considered as thermorheologically simple material; therefore, the physical aging effect was carried through the time shift factor. Different aging parameters were calibrated for the shear and transverse directions. Combined carbon fiber and thermoplastic polyamide resin laminates were tested and were predicted. The predicted results showed good agreement with the experimental data. Hu and Sun (2000) studied the physical aging effect within a linear viscoelastic range of IM7/977-3 carbon/epoxy composites. Several off-axis coupons were tested under different aging time. Experimental data showed different physical aging effects on the elastic and creep compliances. The transient creep compliance was expressed separately for each aging time and off-axis angle. Shift factors and time shift rates were introduced to create reference master curves in term of the effective compliances.

Micromechanical viscoelastic models, that explicitly recognize the multi-axial stress state of the constituents, are unique because the time-dependent behavior is exclusively attributed to the polymeric matrix. Furthermore, they can offer a clear advantage over homogenized anisotropic viscoelastic models by calibrating one or two compliance kernels due to the isotropic nature of the matrix. In addition, the ability to predict the effective viscoelastic response for different fiber volume fractions (FVFs) is another advantage. Finally, the three-dimensional (3D) micromechanical formulation allows for modeling the response of multi-axial stress states. Schaffer and Adams (1981) used FE models of a unit-cell (UC) with the Schapery model for the matrix to generate the effective nonlinear viscoelastic behavior of unidirectional composites. FE predictions compared well for glass/epoxy under creep transverse compression including cure cycle consideration. Aboudi (1990) and Sadkin and Aboudi (1989) applied the Schapery nonlinear viscoelastic model for the matrix subcells of the method of cell (MOC). Nonlinear viscoelastic behavior, including thermorheologically complex response to applied cyclic temperatures, were both modeled and were compared with the FE UC results of Schaffer and Adams (1981). Yancey and Pindera (1990) used Aboudi's model to predict the linear creep response of graphite/epoxy. Barbero and Luciano (1995) formulated an analytical model of creep and relaxation responses using the Laplace transformation for composite materials having transversely isotropic fibers and linear viscoelastic matrix. Power law model was used for the matrix phase. A unit cell model of a cylindrical fibers embedded in the matrix medium was periodically distributed in the entire composite. Predictions were compared with experimental data obtained by Yancey and Pindera (1990). Fisher and Brinson (2001) used the Mori–Tanaka micromechanical theory with viscoelastic formulations and considered the viscoelastic interphase between the fiber and matrix.

In this study the Aboudi (1991) four-subcell micromechanical model is reformulated and cast in an incremental form in order to derive the effective nonlinear viscoelastic response of unidirectional composites and integrated it as a constitutive model within a displacement-based FE. This was previously introduced in the case of pultruded composites (Haj-Ali and Muliana, 2003). In this paper, nonlinear viscoelastic behavior in laminated composites is addressed. The incremental and algorithm formulation at both the microlevel and for the matrix constituents are addressed in detail in the first part. A recursive–iterative integration method applied for the Schapery nonlinear 3D model is used for the isotropic matrix in the proposed micromodel. The second part of this paper includes examining the above formulation by modeling and predicting the nonlinear viscoelastic response for different composite material systems. Off-axis experimental data performed on glass/epoxy (Lou and Schapery, 1971) and T300/5208 graphite/epoxy (Tuttle and Brinson, 1986) are used for this purpose. Physical aging effect is also incorporated in the proposed micromodel. Experimental data on IM7/977-3 carbon/epoxy composites performed by Hu and Sun (2000) are used for calibration and prediction. Finally, the last part deals with FE viscoelastic structural models including creep buckling analyses.

2. A numerical integration method for the Schapery isotropic material model

A multi-axial nonlinear viscoelastic constitutive model for an isotropic polymeric matrix is formulated in this section. The Schapery (1969) single integral constitutive model is used for this purpose. It can be expressed as

$$\begin{aligned}\varepsilon^t &\equiv \varepsilon(t) = g_0^{\sigma^t} D_0 \sigma^t + g_1^{\sigma^t} \int_0^t \Delta D^{(\psi^t - \psi^\tau)} \frac{\mathrm{d}\left(g_2^{\sigma^\tau}\sigma^\tau\right)}{\mathrm{d}\tau}\mathrm{d}\tau \\ \psi^t &\equiv \psi(t) = \int_0^t \frac{\mathrm{d}\xi}{a_\sigma^{\sigma^\xi} a_T^{\mathrm{T}} a_e}\end{aligned} \tag{1}$$

where D_0 is the instantaneous uniaxial elastic compliance, ΔD is the uniaxial transient compliance, g_0, g_1, g_2, and a_σ are the nonlinear viscoelastic parameters. The parameters a_σ, a_T, and a_e are the stress, temperature, and aging time-scaling factors, respectively. The term ψ is used to express the reduced-time. The upper right superscript of a given term is used to denote a dependent variable of this term or function. In general, the nonlinear material parameters: g_0, g_1, g_2, a_σ, a_T, and a_e can depend on the stress, temperature, moisture, among others. These functions are always positive and equal to one in the case of linear viscoelastic behavior. Under fixed environmental conditions, the nonlinear parameters: g_0, g_1, g_2, and a_σ are assumed to be general polynomial functions of the effective octahedral stress. These are generally expressed as

$$\begin{aligned} g_0 &= 1 + \sum_{i=1}^{ng_0} \alpha_i \left\langle \frac{\sigma_{\mathrm{eq}}}{\tau_0} \right\rangle^i \quad g_1 = 1 + \sum_{i=1}^{ng_1} \beta_i \left\langle \frac{\sigma_{\mathrm{eq}}}{\tau_0} \right\rangle^i \\ g_2 &= 1 + \sum_{i=1}^{ng_2} \gamma_i \left\langle \frac{\sigma_{\mathrm{eq}}}{\tau_0} \right\rangle^i \quad a_\sigma = 1 + \sum_{i=1}^{na_\xi} \delta_i \left\langle \frac{\sigma_{\mathrm{eq}}}{\tau_0} \right\rangle^i \\ \psi^t &= \frac{t}{a_\sigma}; \langle x \rangle = \begin{cases} x, & x > 0 \\ 0, & x \leqslant 0 \end{cases}; \quad \sigma_{\mathrm{eq}}^2 = \frac{3}{2} S_{ij} S_{ij} \end{aligned} \tag{2}$$

where $(\alpha_i, \beta_i, \gamma_i, \delta_i,\ i = 1, \ldots, n_{\mathrm{g}})$ are the calibration coefficients and τ_0 is the effective stress limit that determines the end of the linear viscoelastic range.

The uniaxial integral in Eq. (1) can be generalized to describe the multi-axial (3D) strain–stress relations for an isotropic medium. Furthermore, the deviatoric and volumetric parts are decoupled. The deviatoric and volumetric strains in the 3D case are written as

$$e_{ij}^t = \frac{1}{2} g_0^t J_0 S_{ij}^t + \frac{1}{2} g_1^t \int_0^t \Delta J^{(\psi^t - \psi^\tau)} \frac{\mathrm{d}\left(g_2^\tau S_{ij}^\tau\right)}{\mathrm{d}\tau}\mathrm{d}\tau \tag{3}$$

$$\varepsilon_{kk}^t = \frac{1}{3} g_0^t B_0 \sigma_{kk}^t + \frac{1}{3} g_1^t \int_0^t \Delta B^{(\psi^t - \psi^\tau)} \frac{\mathrm{d}\left(g_2^\tau \sigma_{kk}^\tau\right)}{\mathrm{d}\tau}\mathrm{d}\tau \tag{4}$$

where J_0 and B_0 are the instantaneous elastic shear and bulk compliances, respectively. The terms ΔJ and ΔB are the transient shear and bulk compliances, respectively. Next, we further assume that the matrix Poisson's ratio, v, is time independent. This allows using the same nonlinear and transient parameters for the 3D case in a single integral relation as

$$\begin{aligned}\varepsilon_{ij}^t &= e_{ij}^t + \frac{1}{3}\varepsilon_{kk}^t\delta_{ij} \\ &= (1+v)D_0 g_0^t S_{ij}^t + (1+v)g_1^t \int_0^t \Delta D^{(\psi^t-\psi^\tau)} \frac{\mathrm{d}(g_2^\tau S_{ij}^\tau)}{\mathrm{d}\tau}\mathrm{d}\tau \\ &\quad + \frac{(1-2v)}{3}\delta_{ij}\left[D_0 g_0^t \sigma_{kk}^t + g_1^t \int_0^t \Delta D^{(\psi^t-\psi^\tau)} \frac{\mathrm{d}(g_2^\tau \sigma_{kk}^t)}{\mathrm{d}\tau}\mathrm{d}\tau\right]\end{aligned} \tag{5}$$

Comparing the terms in Eqs. (3) and (4) with those in Eq. (5) yields:

$$\begin{aligned}&J_0 = 2(1+v)D_0 \quad B_0 = 3(1-2v)D_0 \\ &\Delta J(\psi) = 2(1+v)\Delta D(\psi) \quad \Delta B(\psi) = 3(1-2v)\Delta D(\psi)\end{aligned} \tag{6}$$

Haj-Ali and Muliana (2004) proposed a recursive–iterative method to integrate the Schapery nonlinear constitutive relation in Eq. (5). A summary of this formulation is presented in Appendix A for completion. Stress components are chosen as the independent state variables. The formulation further assumes that the incremental strain rate is known and fixed for each increment.

2.1. Isothermal physical aging effect on creep behavior

In this section, the previous viscoelastic nonlinear constitutive model is generalized to include physical aging which can have different effects on both the elastic and transient creep compliances. Therefore, the elastic and transient creep response due to aging are characterized independently. The material becomes stiffer during the aging process (Struik, 1978), and an exponential function in term of aging time can be chosen to model the changes in the material stiffness. It is assumed in this study that there is no physical aging effect on the Poisson's ratio. The transient creep strain that carries the aging effect is computed in the effective time-scale domain, λ, as proposed by Struik (1978). The strains can be mapped back to the real time scale, t, to predict the long-term creep response due to physical aging.

The time interval, $\mathrm{d}t$, is related to the effective time interval, $\mathrm{d}\lambda$, by the acceleration factor, a_{t_e}, which can be expressed, at any time as

$$\mathrm{d}\lambda = a_{t_e}(t)\mathrm{d}t \tag{7}$$

$$a_{t_e}(t) = \left(\frac{t_e}{t_e + t}\right)^{\mu} \tag{8}$$

where t_e is the aging time at the start of the test, measured from the time when the material is rapidly cooled down below its glass transition temperature, T_g. The momentary creep compliance curve can be constructed through horizontal shifting in the logarithmic scale of creep compliance curves at different aging times. The logarithmic shift rate, μ, is defined as

$$\mu = -\frac{\mathrm{d}\log a_{t_e}}{\mathrm{d}\log t_e} \tag{9}$$

The total effective time is then reduced to

$$\lambda = \int_0^t a_{t_e}(\xi)\,\mathrm{d}\xi \quad \lambda = \begin{cases} t_e \ln\left(1+\frac{t}{t_e}\right), & \mu = 1 \\ \frac{t_e}{1-\mu}\left[\left(1+\frac{t}{t_e}\right)^{\mu} - 1\right], & \mu \neq 1 \end{cases} \tag{10}$$

where ξ is an integration variable for the time scale.

Following the work by Pasricha et al. (1997), the effect of physical aging is incorporated into the Schapery constitutive model by calculating creep response in the effective time scale, λ. Thus, the integrations in Eqs. (3) and (4) are carried over the λ domain. The terms, which are involving the current incremental time, Δt, are mapped to the incremental effective time, $\Delta\lambda$. The hereditary integrals (Eqs. (A.6) and (A.7)) are expressed, at the end of the current effective time λ by

$$q^{\lambda}_{ij,n} = \exp[-\lambda_n \Delta\psi^{\lambda}] q^{\lambda-\Delta\lambda}_{ij,n} + \left(g^t_2 S^t_{ij} - g^{t-\Delta t}_2 S^{t-\Delta t}_{ij}\right) \frac{1-\exp[-\lambda_n \Delta\psi^{\lambda}]}{\lambda_n \Delta\psi^{\lambda}} \tag{11}$$

$$q^{\lambda}_{kk,n} = \exp[-\lambda_n \Delta\psi^{\lambda}] q^{\lambda-\Delta\lambda}_{kk,n} + \left(g^t_2 \sigma^t_{kk} - g^{t-\Delta t}_2 \sigma^{t-\Delta t}_{kk}\right) \frac{1-\exp[-\lambda_n \Delta\psi^{\lambda}]}{\lambda_n \Delta\psi^{\lambda}} \tag{12}$$

where the reduced effective time increment is

$$\begin{aligned} \Delta\psi^{\lambda} &\equiv \psi^{\lambda} - \psi^{\lambda-\Delta\lambda} \\ \psi^{\lambda} &= \int_0^{\lambda} \frac{\mathrm{d}\xi}{a_\sigma a_T} \end{aligned} \tag{13}$$

The deviatoric and volumetric creep strains in Eqs. (A.9) and (A.10) are rewritten to incorporate the physical aging effect as

$$\begin{aligned} e^t_{ij} = \frac{1}{2}\Bigg[g^t_0 J_0 + g^t_1 g^t_2 \sum_{n=1}^{N} J_n - g^t_1 g^t_2 \sum_{n=1}^{N} J_n \frac{1-\exp[-\lambda_n \Delta\psi^{\lambda}]}{\lambda_n \Delta\psi^{\lambda}} \Bigg] S^t_{ij} - \frac{1}{2} g^t_1 \sum_{n=1}^{N} J_n \Bigg[\exp[-\lambda_n \Delta\psi^{\lambda}] q^{\lambda-\Delta\lambda}_{ij,n} \\ - g^{t-\Delta t}_2 \frac{1-\exp[-\lambda_n \Delta\psi^{\lambda}]}{\lambda_n \Delta\psi^{\lambda}} S^{t-\Delta t}_{ij} \Bigg] \end{aligned} \tag{14}$$

$$\begin{aligned} \varepsilon^t_{kk} = \frac{1}{3}\Bigg[g^t_0 B_0 + g^t_1 g^t_2 \sum_{n=1}^{N} B_n - g^t_1 g^t_2 \sum_{n=1}^{N} B_n \frac{1-\exp[-\lambda_n \Delta\psi^{\lambda}]}{\lambda_n \Delta\psi^{\lambda}} \Bigg] \sigma^t_{kk} - \frac{1}{3} g^t_1 \sum_{n=1}^{N} B_n \Bigg[\exp[-\lambda_n \Delta\psi^{\lambda}] q^{\lambda-\Delta\lambda}_{kk,n} \\ - g^{t-\Delta t}_2 \frac{1-\exp[-\lambda_n \Delta\psi^{\lambda}]}{\lambda_n \Delta\psi^{\lambda}} \sigma^{t-\Delta t}_{kk} \Bigg] \end{aligned} \tag{15}$$

3. Micromechanical formulation

It is assumed that for a given heterogeneous periodic medium, it is possible to define a basic unit-cell (UC) that represents its major geometrical and material characteristics. Each UC is divided into a number of subcells. Traction continuity at an interface between the subcells is enforced using the average stresses of each subcell. The strain compatibility is also expressed in terms of the average strains. This class of approximate micromechanical models is referred herein as constant deformation cell (CDC) micromodels. The subcell strain-interaction matrix, B^{α}, which relates the subcell average strain increment vector, $\mathrm{d}\varepsilon^{\alpha}$, to the overall UC average strain increment, $\mathrm{d}\varepsilon$, is defined as

$$\mathrm{d}\varepsilon^{(\alpha)} = B^{(a)} \mathrm{d}\bar{\varepsilon} \quad \text{where } \mathrm{d}\bar{\varepsilon} = \frac{1}{V} \sum_{\alpha=1}^{\mathrm{Ns}} v^{(\alpha)} \mathrm{d}\varepsilon^{(\alpha)} \tag{16}$$

where α is the subcell number, V is the UC total volume, v^{α} is the subcell volume, and an overbar denotes an overall average quantity over the unit cell. The strain-interaction matrices can be determined by solving the

UC's governing equations, including the traction and compatibility along with the incremental stress–strain relations. The incremental UC average stresses are expressed as

$$\mathrm{d}\overline{\sigma} = \frac{1}{V}\sum_{\alpha=1}^{\mathrm{Ns}} v^{(\alpha)}\,\mathrm{d}\sigma^{(\alpha)} = \frac{1}{V}\sum_{\alpha=1}^{\mathrm{Ns}} v^{(\alpha)} C^{(\alpha)} B^{(\alpha)}\,\mathrm{d}\overline{\varepsilon} = \overline{C}\,\mathrm{d}\overline{\varepsilon} \tag{17}$$

where C^{α} is the current tangent stiffness matrix of the subcell and $\overline{C}$ is the UC effective tangent stiffness matrix. In order to derive the strain-interaction matrices for a UC, the traction and displacement continuity conditions must be imposed, and stress–strain relations must be invoked. It can be shown that a subcell strain-interaction matrix is a function of subcell tangent stiffness and the relative volumes from all subcells.

A four-cell micromodel is derived next using the method of cells (MOC), Aboudi (1991). Aboudi's model has been shown to be well suited for highly nonlinear matrix response, such as that exhibited by metal matrix composites. However, integration of the MOC formulation in general 3D analysis of composite structures has been limited, perhaps because of the large computational effort that is needed. Therefore, it is important to develop efficient stress update and correction algorithms for this model that are suitable for nonlinear structural analysis. In this section, an incremental formulation of Aboudi's model is presented in terms of the average stresses and strains in the subcells. New stress update and correction algorithms are developed. These can significantly reduce the computational effort that is needed when using this micromodel. The new algorithms are formulated given a constant average strain rate for each time step, which make them suitable for integration with FE constitutive framework.

The micromechanical model is shown in Fig. 1. The unidirectional composite, which consists of long fibers arranged unidirectionally in the matrix system, is idealized as doubly periodic array of fibers with rectangular cross section. A quarter UC that consists of four subcells is modeled due to symmetry. The first subcell is a fiber constituent, while subcells 2, 3, and 4 represent the matrix constituents. The long fibers are aligned in the x_1 direction. The other cross-section directions are referred to as the transverse directions. The x_3 direction is called the out-of plane axis or lamina thickness direction. The total volume of the UC is taken to be equal to one. The volumes of the four subcells are

$$V_1 = bh \quad V_2 = h(1-b) \quad V_3 = b(1-h) \quad V_4 = (1-b)(1-h) \tag{18}$$

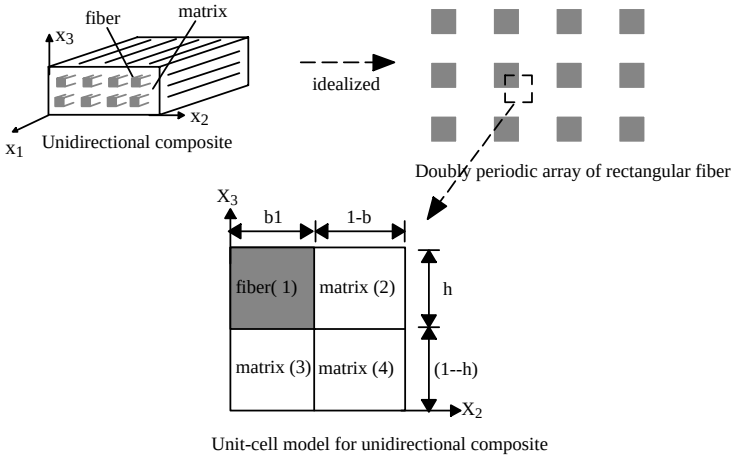

Fig. 1. Micromodel of unidirectional composites.

The notations used for the stress and strain vectors are

$$\begin{aligned} \mathrm{d}\sigma_k^{(\alpha)} &= \{\mathrm{d}\sigma_{11}, \mathrm{d}\sigma_{22}, \mathrm{d}\sigma_{33}, \mathrm{d}\tau_{12}, \mathrm{d}\tau_{13}, \mathrm{d}\tau_{23}\} \quad \alpha = 1, \ldots, 4 \\ \mathrm{d}\varepsilon_k^{(\alpha)} &= \{\mathrm{d}\varepsilon_{11}, \mathrm{d}\varepsilon_{22}, \mathrm{d}\varepsilon_{33}, \mathrm{d}\gamma_{12}, \mathrm{d}\gamma_{13}, \mathrm{d}\gamma_{23}\} \quad k = 1, \ldots, 6 \end{aligned} \tag{19}$$

The 3D nonlinear constitutive integration for the fiber and matrix constituents is performed separately for each subcell. The fiber is linear elastic and transversely isotropic, while the matrix medium is viscoelastic. The homogenization of the micromodel should satisfy displacement and traction continuity. Perfect bond is assumed along the interfaces of the subcells. In the fiber direction, the four subcells satisfy the same strain continuity relation. The axial average stress definition is used as a second independent relation in order to relate the effective axial stress to the stresses in the subcells. The following equations summarize the relations in the axial mode:

$$\begin{aligned} &\mathrm{d}\varepsilon_1^{(1)} = \mathrm{d}\varepsilon_1^{(2)} = \mathrm{d}\varepsilon_1^{(3)} = \mathrm{d}\varepsilon_1^{(4)} = \mathrm{d}\overline{\varepsilon}_1 \\ &V_1\,\mathrm{d}\sigma_1^{(1)} + V_2\,\mathrm{d}\sigma_1^{(2)} + V_3\,\mathrm{d}\sigma_1^{(3)} + V_4\,\mathrm{d}\sigma_1^{(4)} = \mathrm{d}\overline{\sigma}_1 \end{aligned} \tag{20}$$

where overbar denotes an overall average quantity over the unit cell.

Along the interfaces between the subcells with normal in the x_2 direction, the in-plane stress components σ_{22} and τ_{12} must satisfy traction continuity conditions. The total strain components ε_{22} and γ_{12} from subcells 1 and 2, and subcells 3 and 4, respectively should also satisfy strain compatibility conditions. These relations are written in an incremental form as

$$\begin{aligned} &\mathrm{d}\sigma_2^{(1)} = \mathrm{d}\sigma_2^{(2)} \\ &\mathrm{d}\sigma_2^{(3)} = \mathrm{d}\sigma_2^{(4)} \\ &\frac{V_1}{V_1+V_2}\,\mathrm{d}\varepsilon_2^{(1)} + \frac{V_2}{V_1+V_2}\,\mathrm{d}\varepsilon_2^{(2)} = \mathrm{d}\overline{\varepsilon}_2 \\ &\frac{V_3}{V_3+V_4}\,\mathrm{d}\varepsilon_2^{(3)} + \frac{V_4}{V_3+V_4}\,\mathrm{d}\varepsilon_2^{(4)} = \mathrm{d}\overline{\varepsilon}_2 \end{aligned} \tag{21}$$

$$\begin{aligned} &\mathrm{d}\sigma_4^{(1)} = \mathrm{d}\sigma_4^{(2)} \\ &\mathrm{d}\sigma_4^{(3)} = \mathrm{d}\sigma_4^{(4)} \\ &\frac{V_1}{V_1+V_2}\,\mathrm{d}\varepsilon_4^{(1)} + \frac{V_2}{V_1+V_2}\,\mathrm{d}\varepsilon_4^{(2)} = \mathrm{d}\overline{\varepsilon}_4 \\ &\frac{V_3}{V_3+V_4}\,\mathrm{d}\varepsilon_4^{(3)} + \frac{V_4}{V_3+V_4}\,\mathrm{d}\varepsilon_4^{(4)} = \mathrm{d}\overline{\varepsilon}_4 \end{aligned} \tag{22}$$

Considering interfaces between subcells with normal in the x_3 direction, the out-of-plane stress components σ_{33} and τ_{13} must satisfy traction continuity conditions. The total strain components ε_{33} and γ_{13} from subcells 1 and 3, and subcells 2 and 4, respectively, should also satisfy strain compatibility conditions. These relations are expressed in incremental form as

$$\begin{aligned} &\mathrm{d}\sigma_3^{(1)} = \mathrm{d}\sigma_3^{(3)} \\ &\mathrm{d}\sigma_3^{(2)} = \mathrm{d}\sigma_3^{(4)} \\ &\frac{V_1}{V_1+V_3}\,\mathrm{d}\varepsilon_3^{(1)} + \frac{V_3}{V_1+V_3}\,\mathrm{d}\varepsilon_3^{(3)} = \mathrm{d}\overline{\varepsilon}_3 \\ &\frac{V_2}{V_2+V_4}\,\mathrm{d}\varepsilon_3^{(2)} + \frac{V_4}{V_2+V_4}\,\mathrm{d}\varepsilon_3^{(4)} = \mathrm{d}\overline{\varepsilon}_3 \end{aligned} \tag{23}$$

$$
\begin{aligned}
&\mathrm{d}\sigma_5^{(1)} = \mathrm{d}\sigma_5^{(3)} \\
&\mathrm{d}\sigma_5^{(2)} = \mathrm{d}\sigma_5^{(4)} \\
&\frac{V_1}{V_1+V_3}\,\mathrm{d}\varepsilon_5^{(1)} + \frac{V_3}{V_1+V_3}\,\mathrm{d}\varepsilon_5^{(3)} = \mathrm{d}\bar{\varepsilon}_5 \\
&\frac{V_2}{V_2+V_4}\,\mathrm{d}\varepsilon_5^{(2)} + \frac{V_4}{V_2+V_4}\,\mathrm{d}\varepsilon_5^{(4)} = \mathrm{d}\bar{\varepsilon}_5
\end{aligned}
\tag{24}
$$

Finally, both types of interfaces should satisfy transverse shear stress continuity. Therefore, the transverse shear stresses in the four subcells are equal to the effective transverse shear stress. The transverse shear strains from the four subcells in the average strain definition are used to express the relations with the effective transverse shear strain of the UC. The transverse shear relations are summarized as

$$
\begin{aligned}
&\mathrm{d}\sigma_6^{(1)} = \mathrm{d}\sigma_6^{(2)} = \mathrm{d}\sigma_6^{(3)} = \mathrm{d}\sigma_6^{(4)} = \mathrm{d}\bar{\sigma}_6 \\
&V_1\,\mathrm{d}\varepsilon_6^{(1)} + V_2\,\mathrm{d}\varepsilon_6^{(2)} + V_3\,\mathrm{d}\varepsilon_6^{(3)} + V_4\,\mathrm{d}\varepsilon_6^{(4)} = \mathrm{d}\bar{\varepsilon}_6
\end{aligned}
\tag{25}
$$

Eqs. (20)–(25) along with the stress–strain relations within each fiber and matrix subcells complete the micromechanical formulation of the unidirectional lamina. These relations are used in incremental (rate) form due to the nonlinear constitutive relations in the matrix subcells. Next, the strain components in the subcells are grouped into two parts: (a) and (b). The first part corresponds to the incremental compatibility equations and the second part is the traction continuity relations (homogeneous equations). The two groups of strain vectors are defined by

$$
\underset{(1\times 13)}{\mathrm{d}\varepsilon_a^{\mathrm{T}}} = \left\{\mathrm{d}\varepsilon_1^{(1)}, \mathrm{d}\varepsilon_1^{(2)}, \mathrm{d}\varepsilon_1^{(3)}, \mathrm{d}\varepsilon_1^{(4)}, \mathrm{d}\varepsilon_2^{(1)}, \mathrm{d}\varepsilon_2^{(3)}, \mathrm{d}\varepsilon_4^{(1)}, \mathrm{d}\varepsilon_4^{(3)}, \mathrm{d}\varepsilon_3^{(1)}, \mathrm{d}\varepsilon_3^{(2)}, \mathrm{d}\varepsilon_5^{(1)}, \mathrm{d}\varepsilon_5^{(2)}, \mathrm{d}\varepsilon_6^{(1)}\right\} \tag{26}
$$

and

$$
\underset{(1\times 11)}{\mathrm{d}\varepsilon_b^{\mathrm{T}}} = \left\{\mathrm{d}\varepsilon_2^{(2)}, \mathrm{d}\varepsilon_2^{(4)}, \mathrm{d}\varepsilon_4^{(2)}, \mathrm{d}\varepsilon_4^{(4)}, \mathrm{d}\varepsilon_3^{(3)}, \mathrm{d}\varepsilon_3^{(4)}, \mathrm{d}\varepsilon_5^{(3)}, \mathrm{d}\varepsilon_5^{(4)}, \mathrm{d}\varepsilon_6^{(2)}, \mathrm{d}\varepsilon_6^{(3)}, \mathrm{d}\varepsilon_6^{(4)}\right\} \tag{27}
$$

The set of equations (20)–(25), can be expressed in terms of the strain increments in the subcells after substituting the incremental stress–strain relations. The rearrangement of the strain increments allows this set to be transformed into:

$$
\begin{Bmatrix} \underset{(13\times 1)}{\mathrm{d}R_\varepsilon} \\ \hline \underset{(11\times 1)}{\mathrm{d}R_\sigma} \end{Bmatrix} = \begin{bmatrix} \underset{(13\times 13)}{I} & \underset{(13\times 11)}{\overline{A}_{ab}} \\ \hline \underset{(11\times 13)}{\overline{A}_{ba}} & \underset{(11\times 11)}{\overline{A}_{bb}} \end{bmatrix} \begin{Bmatrix} \underset{(13\times 1)}{\mathrm{d}\varepsilon_a} \\ \hline \underset{(11\times 1)}{\mathrm{d}\varepsilon_b} \end{Bmatrix} - \begin{bmatrix} \underset{(13\times 6)}{\overline{D}_a} \\ \hline \underset{(11\times 6)}{0} \end{bmatrix} \left\{ \underset{(6\times 1)}{\mathrm{d}\bar{\varepsilon}} \right\} \tag{28}
$$

where $\mathrm{d}R_\sigma$ is the residual form of the stress relations (traction continuity) expressed incrementally in terms of the strains in the subcells. The matrices that appear in Eq. (28) are listed below and can be identified by examining Eqs. (18)–(25). The nonzero terms of $\overline{A}_{ab}$ are

$$
\begin{aligned}
&\overline{A}_{ab}(5,1) = \overline{A}_{ab}(6,2) = \overline{A}_{ab}(7,3) = \overline{A}_{ab}(8,4) = \overline{A}_{ab}(13,9) = \frac{1-h}{h} \\
&\overline{A}_{ab}(9,5) = \overline{A}_{ab}(10,6) = \overline{A}_{ab}(11,7) = \overline{A}_{ab}(12,8) = \overline{A}_{ab}(13,10) = \frac{1-b}{b} \\
&\overline{A}_{ab}(13,11) = \frac{1-b1-h}{bh}
\end{aligned}
\tag{29}
$$

The nonzero terms of $\overline{D}_a$ are

$$\begin{aligned}
&\overline{D}_a(1,1) = \overline{D}_a(2,1) = \overline{D}_a(3,1) = \overline{D}_a(4,1) = 1 \\
&\overline{D}_a(5,2) = \overline{D}_a(6,2) = \overline{D}_a(7,4) = \overline{D}_a(8,4) = \frac{1}{h} \\
&\overline{D}_a(9,3) = \overline{D}_a(10,3) = \overline{D}_a(11,5) = \overline{D}_a(12,5) = \frac{1}{b} \\
&\overline{D}_a(9,3) = \frac{1}{bh}
\end{aligned} \tag{30}$$

The terms of $\overline{A}_{ba}$ and $\overline{A}_{bb}$ matrices can be found in Appendix B. Only the inverse of the (11×11) submatrix in Eq. (28) is needed to solve for $\mathrm{d}\varepsilon_a$ and $\mathrm{d}\varepsilon_b$. The strain-concentration matrices are determined by solving $\mathrm{d}R_\sigma = 0$ and $\mathrm{d}R_\varepsilon = 0$ equations.

The micromechanical relations are exact only in the case of linear stress–strain relations in the fiber and matrix subcells. Due to the nonlinear response in one or more of the subcells, the incremental relations will usually violate the constitutive equations. Thus, an iterative correction scheme is needed in order to satisfy both the micromechanical constraints and the constitutive equations. The tasks for the micromechanical algorithm can be states as: given history variables in the subcells from previous converged solution and a constant average strain rate for the unit-cell within the current time increment, update the effective stress, effective stiffness, and the history variables at the end of the increment, as illustrated in Fig. 2.

3.1. Multi-scale structural framework

A general 3D multi-scale framework is proposed for the nonlinear analysis of laminated composite structures. Fig. 3 illustrates the proposed analysis framework for multi-layered structures using both 3D or shell based FE models. In the case of 3D elements, the sublaminate model (Pecknold and Haj-Ali, 1993, Haj-Ali et al., 1993) represents the nonlinear effective response at each material point (Gaussian point). In the case of shell elements, each layer is explicitly modeled with one or more integration points under plane stress condition and the sublaminate model is reduced to the classical lamination theory in this case. Constant transverse-shear cross-sectional stiffness is assumed for the shell elements. This assumption is valid in the cases where the transverse stresses in the different layers are very small compared to the in-plane stresses. The 3D micromechanical models provide for the effective nonlinear constitutive behavior for each Gaussian point. The shell element's effective through-thickness response is generated at select integration points on its reference surface by integrating the effective micromechanical response over all Gaussian points as shown in Fig. 3.

A nonlinear material model in a displacement-based FE code is required to update the stresses and the tangent or algorithmic stiffness matrix for a given strain increment. The input data to this subroutine consists of the fiber and matrix material properties, the calibrated viscoelastic parameters for the matrix constituents, lamination sequence, and internal convergence tolerances as well as control flags. Different convergence tolerances are used in the stress update and correction algorithms at the sublaminate, micromechanical, and matrix levels. An allocated storage for the solution dependent state variables (SDV), at each material point (Gaussian point), is used and updated at the end of each convergent increment. This vector contains all the history variables of the model at all levels of hierarchy.

4. Validation of the nonlinear constitutive framework

The proposed modeling framework is examined in its ability to predict the nonlinear viscoelastic behavior of composite materials and structures. The effective response is generated from calibrated in situ

1. Input variables

$$\Delta\bar{\varepsilon}_{ij}^{t} \quad , \bar{\sigma}_{ij}^{t-\Delta t} \qquad \text{Hist}^{t-\Delta t}: \ \varepsilon_{ij}^{(\alpha),\,t-\Delta t} \quad , \sigma_{ij}^{(\alpha),\,t-\Delta t} \quad , \alpha = 1, 2, 3, 4$$

$$q_{ij,n}^{(\beta),\,t-\Delta t} \quad , q_{kk,n}^{(\beta),\,t-\Delta t} \quad , \beta = 2, 3, 4$$

2. Initialize linearized state

$$C^{(\alpha),\,t-\Delta t} = C^{(\alpha),\,t-\Delta t}\left(\text{Hist}^{t-\Delta t}\right)$$

$$B^{(\alpha),\,t,tr} = B^{(\alpha),\,t,tr}\left(\nu^{(\alpha)}, C^{(\alpha),\,t-\Delta t}\right)$$

$$\Delta\varepsilon^{(\alpha),\,t,(0)} = \Delta\varepsilon^{(\alpha),\,t,tr} = B^{(\alpha),\,t,tr}\,\Delta\bar{\varepsilon}^{t}$$

3. Iterate for k=1, 2, 3....

3.1 Evaluate stresses at all subcells

CALL Algorithm in Figure A.1. to get $\sigma_{ij}^{(\alpha),\,t,(k+1)} \quad , C^{(\alpha),\,t,(k)}$

3.2 Compute strain correction

$$\delta\Delta\varepsilon^{(\alpha),t,(k+1)} = \left\{\begin{array}{c}\delta\Delta\varepsilon_a \\ \hline \delta\Delta\varepsilon_b\end{array}\right\}^{t,\,(k+1)} = -\left[\begin{array}{c|c} \mathbf{I} & \bar{A}_{ab} \\ \hline \bar{A}_{ba} & \bar{A}_{bb}\end{array}\right]^{t,\,(k),\,-1}\left\{\begin{array}{c} R_\varepsilon \\ \hline R_\sigma\end{array}\right\}^{t,\,(k)}$$

$$\Delta\varepsilon^{(\alpha),\,t,\,(k+1)} = \Delta\varepsilon^{(\alpha),\,t,\,(k)} + \delta\Delta\varepsilon^{(\alpha),\,t,\,(k+1)}$$

3.3 Evaluate residual vector $R^{t,(k)} = (R_\varepsilon, R_\sigma)$ from Eq. (28).

IF $\| R^{t,(k)} \| \le \text{Tol}$ THEN GOTO 4 and EXIT

ENDIF GOTO 3

4. Update effective stress, consistent tangent stiffness, and history variables

$$\bar{\sigma}_{ij}^{t} \leftarrow \bar{\sigma}_{ij}^{t,(k+1)} \qquad \bar{C}_{ij}^{t} \leftarrow \bar{C}_{ij}^{t,(k+1)}$$

$$\varepsilon_{ij}^{(\alpha),\,t} \leftarrow \varepsilon_{ij}^{(\alpha),\,t,(k+1)} \quad , \sigma_{ij}^{(\alpha),\,t} \leftarrow \sigma_{ij}^{(\alpha),\,t,(k+1)} \quad , \alpha = 1, 2, 3, 4$$

$$q_{ij,n}^{(\beta),\,t} \leftarrow q_{ij,n}^{(\beta),\,t,(k+1)} \quad , q_{kk,n}^{(\beta),\,t} \leftarrow q_{kk,n}^{(\beta),\,t,(k+1)} \quad , \beta = 2, 3, 4$$

Fig. 2. A micromechanical recursive–iterative integration algorithm for nonlinear viscoelastic behavior in laminated composite.

properties of the matrix and fiber constituents. To that end, different creep tests available in the literature are used. Off-axis test results are available for glass/epoxy (Lou and Schapery, 1971) and T300/5208 graphite/epoxy (Tuttle and Brinson, 1986) composites. Prediction of the calibrated model is examined against test results not used in the calibration process.

Lou and Schapery (1971) derived a micromechanical relation for the average matrix stress in a lamina subjected to a plane stress state:

$$\sigma_{yy}^{m} = \sigma_y \quad \sigma_{xx}^{m} = \nu_{\mathrm{m}}\sigma_{yy} \quad \tau_{xy}^{m} = \tau_{xy} \tag{31}$$

where ν_{m} is the matrix Poisson's ratio. The matrix octahedral shear stress in the Schapery viscoelastic integral is used to model the nonlinear behavior of the matrix and hence the composites. Excellent creep and predictions were demonstrated by Lou and Schapery's modeling approach. The current approach is similar but employs a refined 3D micromodel that can ultimately be used in both 2D and 3D structural models.

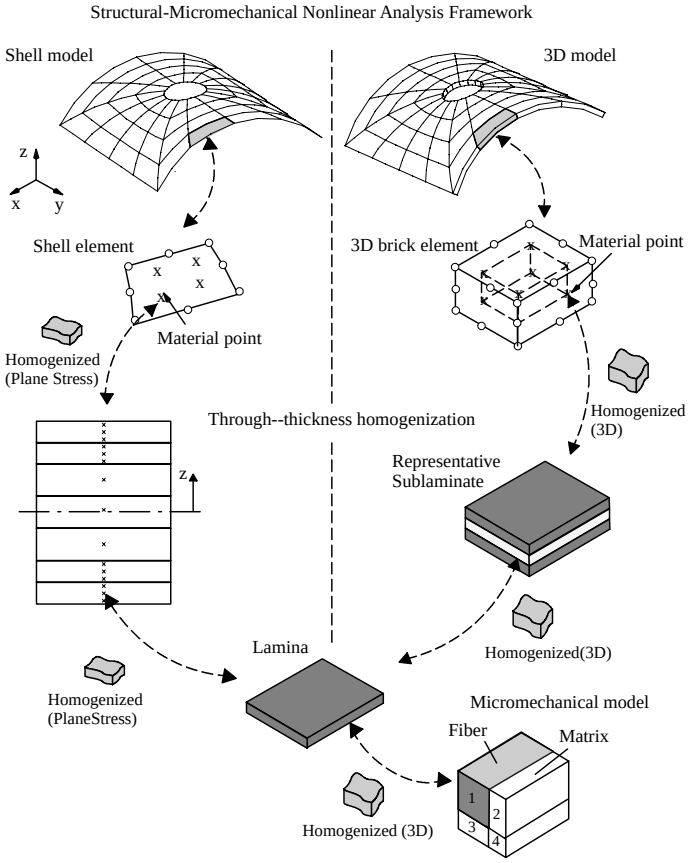

Fig. 3. A multi-scale micromechanical–structural framework for nonlinear viscoelastic analysis of laminated composite structures.

Creep test results on glass/epoxy off-axis composite specimens reported by Lou and Schapery (1971) were used for validation of the current modeling approach. The elastic properties for glass and epoxy are given in Table 1. Linear viscoelastic calibration was performed using results from the 45° off-axis specimen under the lowest applied axial stress (1.382 ksi). The Prony series coefficients were calibrated until the overall response matches with the experimental data. The inverse of the retardation times (λ_n) were chosen as $\lambda_n = 10^{1-n}$. The results from Prony series calibration are shown in Table 2. The limit for the matrix linear viscoelastic response, τ_0 in Eq. (2), was determined from the different linear creep responses to be 1.4 ksi. The viscoelastic parameter g_0 was calibrated using second order polynomial function from the 45° off-axis test for applied stress of 3.448 ksi, as shown in Fig. 4. Other creep responses for the same angle were also monitored during the calibration. The same process was repeated in the calibration of g_2 using the 30°

Table 1
Glass and epoxy elastic material properties, $vf = 0.476$

	E GPa (ksi)	v
Glass fiber	72.4 (10,500)	0.22
Epoxy matrix	4.3 (620)	0.31

Table 2
Calibration Prony series coefficients for the epoxy matrix

n	λ_n (s^{-1})	$D_n \times 10^{-6}$ MPa^{-1} (ksi^{-1})
1	1	2.18 (15.0)
2	10^{-1}	4.87 (33.6)
3	10^{-2}	5.08 (35.0)
4	10^{-3}	6.64 (45.8)
5	10^{-4}	1.83 (12.6)
6	10^{-5}	2.90 (20.0)

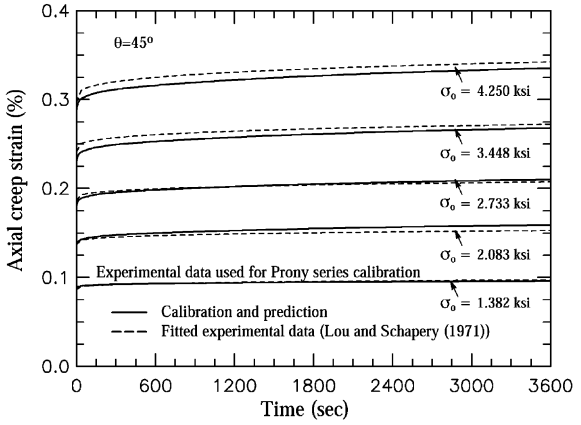

Fig. 4. Axial creep strain for 45° off-axis coupons.

off-axis test results. An effort was made to match the creep in both curves with applied stress levels of 6.897 and 8.058 ksi. Overall the nonlinear calibration strikes a balance between all nonlinear curves as seen in Fig. 5. The calibrated polynomial coefficients are shown in Fig. 6. The parameters g_1 and a_σ are fixed to one. The predicted results are close to the experimental data as shown in Figs. 7 and 8 for 60° and 90° off-axis coupons, respectively.

Another creep tests performed by Tuttle and Brinson (1986) on T300/5208 graphite/epoxy were used to examine the micromodel. Off-axis specimens with 10° and 90° fiber orientations were subjected to 480 min creep tests. The elastic properties for graphite and epoxy are given in Table 3. The effective properties of T300/5208 composites with fiber volume fraction of 0.65 are shown in Table 4. Linear viscoelastic calibration was performed from 10° off-axis coupon under the lowest applied shear stress (2.9 MPa), as shown in Fig. 9. Prony series coefficients with four terms were calibrated, as seen in Table 5. The viscoelastic parameters, g_0, g_2, and a_σ were also calibrated from the 10° off-axis creep results. The calibrated results are shown in Fig. 10. The linear viscoelastic limit of the matrix effective stress, τ_0, was determined as 25 MPa. Good predictions from the proposed micromodel are shown in Figs. 9 and 11 for the shear and transverse creep responses, respectively.

4.1. Effect of physical aging on creep

Hu and Sun (2000) investigated the effect of physical aging on IM7/977-3 graphite/epoxy laminated plates. Physical aging affects both the initial elastic and creep compliances. In this study the physical aging

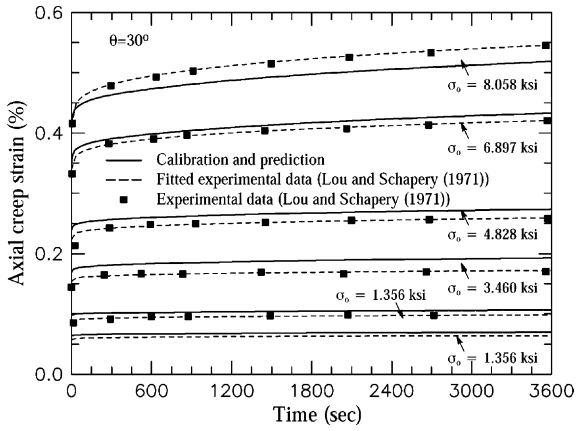

Fig. 5. Axial creep strain for 30° off-axis coupons.

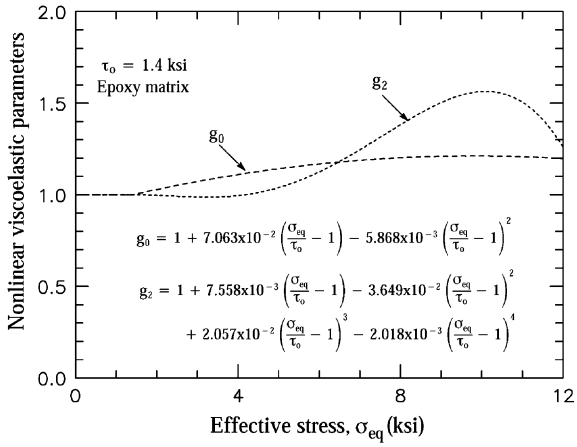

Fig. 6. Nonlinear stress dependent parameters in the Schapery's equations.

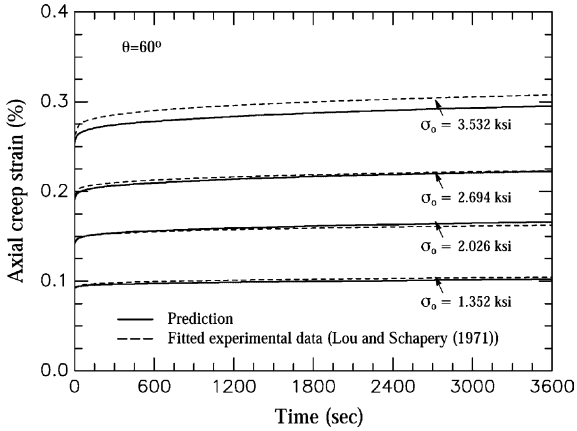

Fig. 7. Axial creep strain for 60° off-axis coupons.

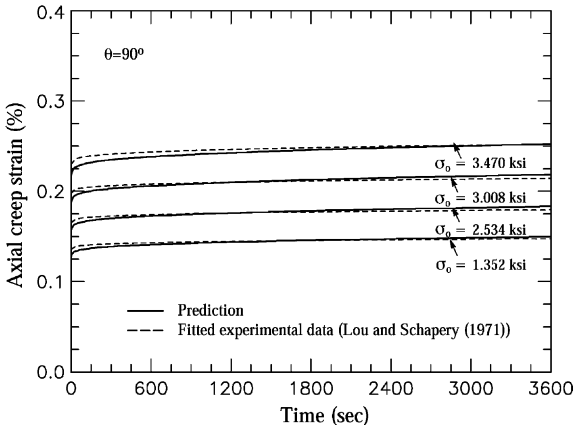

Fig. 8. Axial creep strain for transverse coupons.

Table 3
Elastic material properties for T300-graphite and 5208 epoxy

	GPa (ksi)			v_{12}	v_{23}
	E_{11}	E_{22}	G_{12}		
Fiber (T300-graphite)	200 (29000)	3 (1886)	44 (6382)	0.39	0.40
Matrix (5208 epoxy)	4.6 (667)			0.35	

Table 4
Elastic properties for T300/5208 graphite–epoxy lamina, $vf = 0.65$

	GPa (ksi)			v_{12}	v_{23}
	E_{11}	E_{22}	G_{12}		
Experimental data (Tuttle and Brinson, 1986)	132.2 (19174)	9.434 (1368)	6.410 (930)	0.273	
Micromodel (four-cell model)	131.6 (19087)	9.434 (1368)	6.435 (933)	0.377	0.425

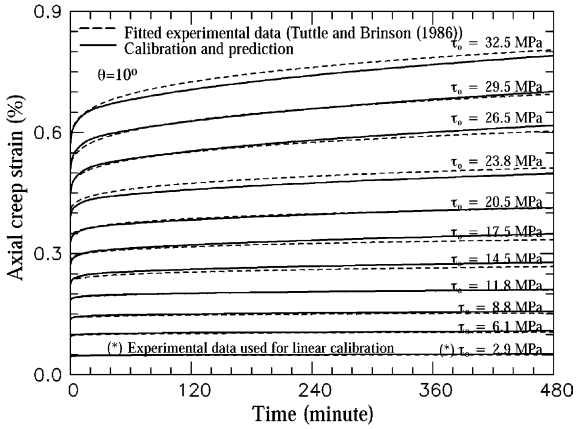

Fig. 9. Shear creep strain from 10° off-axis specimens.

Table 5
Calibrated Prony series coefficients for the 5208 epoxy matrix

n	λ_n (s^{-1})	D_n short-term creep (480 min)$\times 10^{-6}$ MPa^{-1} (ksi^{-1})
1	1	8.50 (58.61)
2	10^{-1}	8.36 (57.64)
3	10^{-2}	5.50 (37.92)
4	10^{-3}	33.80 (233.04)

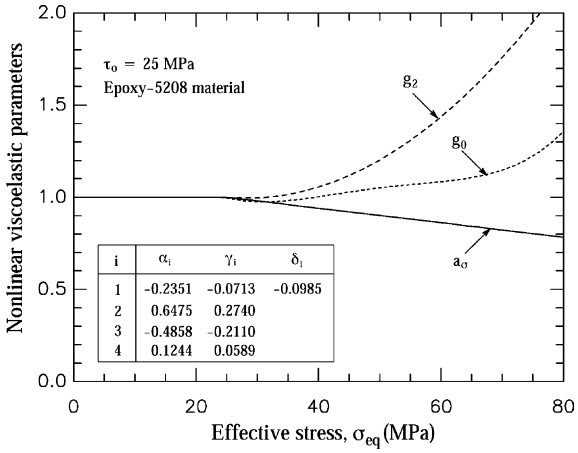

Fig. 10. In situ nonlinear viscoelastic parameters as function of the effective stress for epoxy (5208) matrix.

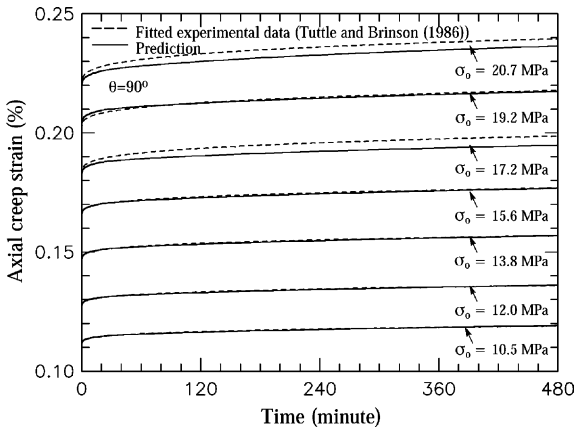

Fig. 11. Transverse creep strain.

effect on the linear creep responses is considered and implemented in the viscoelastic constitutive framework. The experimental data reported by Hu and Sun (2000) is used to calibrate and validate the prediction

of the micromodel with an aging matrix. Four sets of off-axis specimens with different fiber orientations: 15°, 30°, 45°, and 90° were aged for different aging times, t_e: 5, 12, 24, 48, 72, and 96 h. Creep tests were then conducted for times less than 1/10 of their aging time. Relatively low axial tensile loads, with magnitudes: 43.4, 23.5, 19.7, and 15.2 MPa, were applied to the 15°, 30°, 45°, and 90° off-axis coupons, respectively. All tests were under linear viscoelastic range. The glass transition temperature, T_g, of the studied graphite/epoxy composite is 188–193 °C, while the tests were performed at a constant temperature of 104 °C. The linear elastic effective compliances for each off-axis test are shown in Fig. 12. The elastic compliances are defined at aging time $t_e = 5$ h. The compliances in the axial and transverse specimens were used to calibrate the in situ elastic properties of the fiber and matrix. Fig. 12 also shows the predicted effective elastic compliance from the micromodel along with test data for the off-axis specimen. Table 6 includes the calibrated elastic properties for the IM7 fiber and 977-3 matrix used in the micromodel.

Next, the matrix viscoelastic parameters are calibrated to model the aging effect on the elastic and transient creep responses. Elastic and transient creep experimental data are reproduced from the fitted experimental equations of Hu and Sun (2000). Their experimental results show that elastic compliances of all off-axis specimens decrease as aging time increases. Therefore, the matrix Young's modulus in the micromodel is modified to account for the effect of aging time. In this study, a Prony series is used to describe the matrix modulus as a function of aging time:

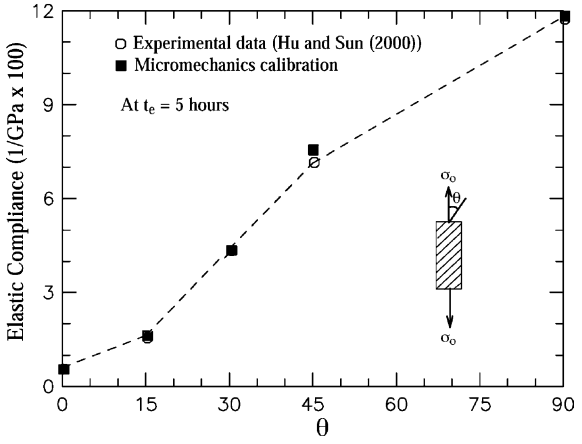

Fig. 12. Elastic compliance from IM7/977-3 off-axis tests at $t_e = 5$ h.

Table 6
Elastic material properties for IM7 fiber and 977-3 matrix

	GPa (ksi)			v_{12}	v_{23}
	E_{11}	E_{22}	G_{12}		
IM7 fiber	256 (37129)	14.6 (2118)	56.6 (8209)	0.25	0.30
977-3 matrix	3.5 (508)			0.25	

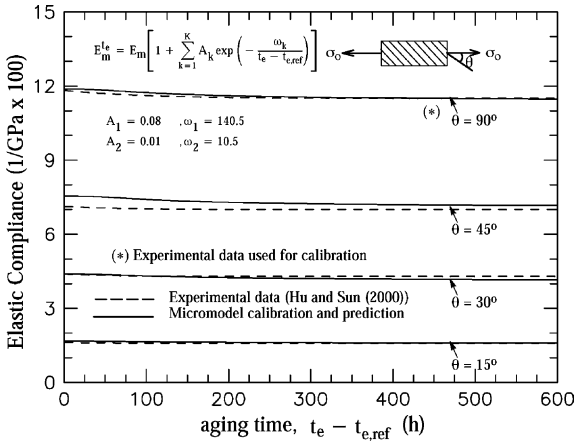

Fig. 13. Predicted elastic compliances for IM7/977-3 off-axis specimens as a function of aging time.

Table 7
Calibrated Prony series coefficients for the 977-3 matrix

n	λ_n (s^{-1})	$D_n \times 10^{-5}$ MPa^{-1} (ksi^{-1})
1	1	1.00 (6.89)
2	10^{-1}	3.36 (23.17)
3	10^{-2}	3.50 (24.13)
4	10^{-3}	4.58 (31.58)
5	10^{-4}	32.60 (224.77)
6	10^{-5}	20.00 (137.89)

$$E_{\mathrm{m}}^{t_e} = E_{\mathrm{m}}\left[1 + \sum_{k=1}^{K} A_k \exp\left(-\frac{\omega_\kappa}{t_e - t_{e,\mathrm{ref}}}\right)\right] \tag{32}$$

where E_{m} is the initial matrix Young's modulus at reference time as shown in Table 6. The terms A_k and ω_k are calibrated from the 90° off-axis coupon tests. Two terms are used in the above equation: $(A_1\omega_1) = (0.08, 140.5)$ and $(A_2\omega_2) = (0.01, 10.5)$. The calibrated and predicted elastic compliances as a function of aging time are shown in Fig. 13 for different off-axis specimens. Good prediction is shown by the micromodel when the aging effect is attributed to the matrix Young's modulus. The transient creep parameters are calibrated from 45° off-axis coupon at the reference aging time, $t_e = 5$ h. Prony series coefficients with six terms are used for the in situ matrix, as seen in Table 7.

The aging shift rate, μ, Eq. (9), is used to characterize the aging effect on the transient creep response. The acceleration factor, a_{t_e}, is characterized at each sampled aging time. The inverse of the acceleration factor a_{t_e}, Eq. (8), is called the aging time-scale factor, a_e, used in Eq. (1). The 45° off-axis creep tests, given at t_e: 12, 24, 48, 72, and 96 h were used to calibrate the matrix aging parameters. An a_e value for the in situ matrix was determined such that the overall creep from the micromodel exactly matches the 45° off-axis creep at each sampled aging time. The calibrated aging time-scale is shown in logarithmic scale in Fig. 14. The slope from a linear regression determines the aging shift rate, μ, which in this case is 0.5827. The calibrated transient creep curves for the five sampled aging times are shown in Fig. 16. The results show

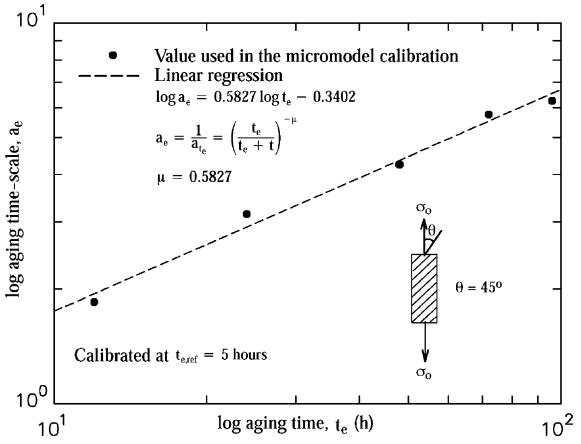

Fig. 14. Logarithmic plot of aging parameter versus aging time.

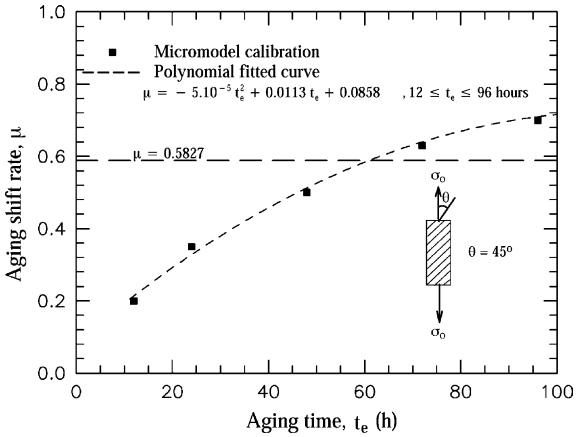

Fig. 15. Shift rate factor versus aging time.

that using a constant aging shift rate is not sufficient to capture the creep response for aging times larger than the reference time. In order to correct this mismatch, the previously calibrated five aging time-scale values are used to yield a separate μ value for each case. Next, the new five μ values were assumed to be part of a polynomial function of t_e. The calibrated aging shift factor is shown in Fig. 15 and it is strongly dependent on aging time. Fig. 16 shows the creep response for 45° off-axis using the new calibrated aging time-scale with the $\mu(t_e)$ polynomial function. In this case the creep response is better matched when using a nonconstant aging shift rate. Next, the creep response is predicted by the micromodel and examined for aged off-axis specimen, $\theta = 15°$, 30°, 45°, and 90°, that are not used in the calibration process. Fig. 17 shows the transient creep strain as a function of time for all off-axis cases taken at different aging times. The proposed aging modeling on the matrix in the micromodel is capable of capturing the overall multi-axial creep-aging effect on the matrix.

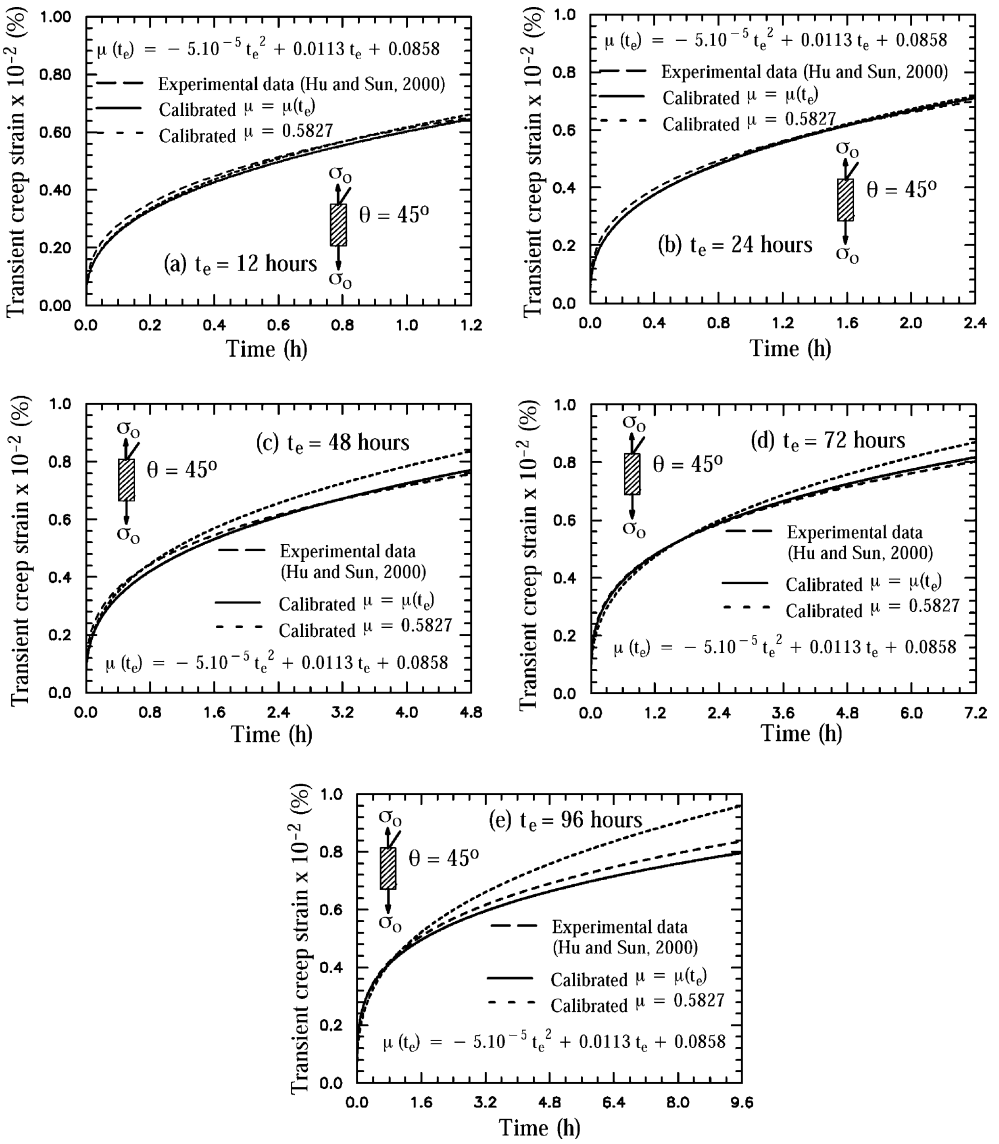

Fig. 16. Calibrated creep strain from 45° off-axis coupon at various aging time.

5. FE structural applications

Having established the efficiency and accuracy of the proposed nonlinear viscoelastic micromodels, we proceed to implement this framework within a general purposed FE code. The material subroutine (UMAT) in the ABAQUS (2002) FE code is used for this purpose. As previously described in Fig. 3, two FE modeling approaches can be used for laminated composite structures. The first using shell based elements, where each layer is explicitly modeled with a micromodel during the nonlinear analysis. The second approach employs 3D continuum brick elements with a sublaminate model used for the homogeneous

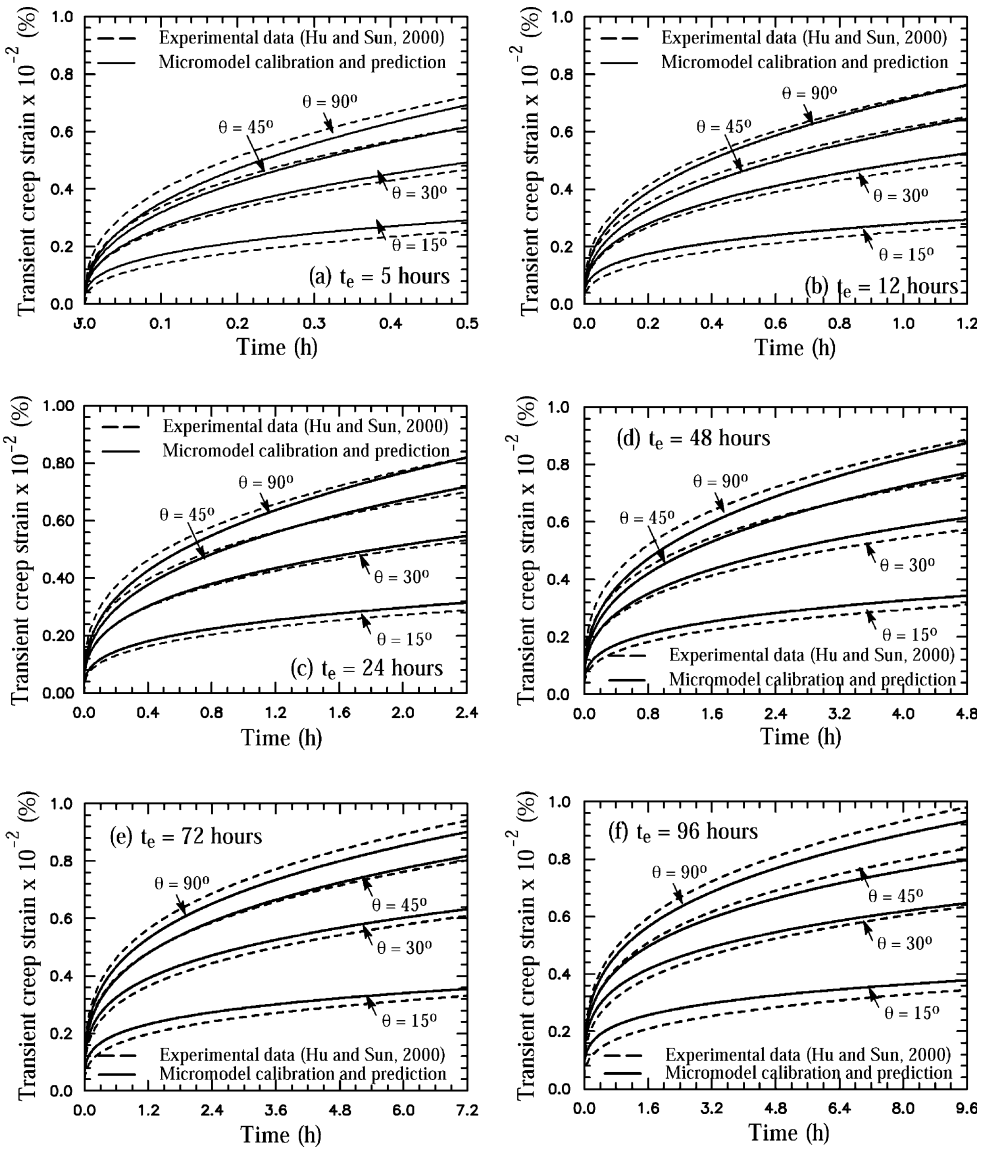

Fig. 17. Predicted creep strain for off-axis coupons at different aging hours.

nonlinear effective response of a repeating stacking sequence. In the following, two examples are presented to demonstrate the integrated micromechanical–structural viscoelastic analysis method using layered shell elements.

The first example is concerned with the viscoelastic response of composite panel subjected to an external uniform pressure. Fig. 18 shows the geometry, boundary conditions, and the FE mesh of the panel along with the layup used through the thickness. A total of 512 quadratic shell elements with 9 nodes and reduced integration (S9R5) are used in the model. The material used for each layer is the T300/5208 graphite/epoxy, where the elastic properties for the fiber and matrix are listed in Table 3. Originally, the Prony series

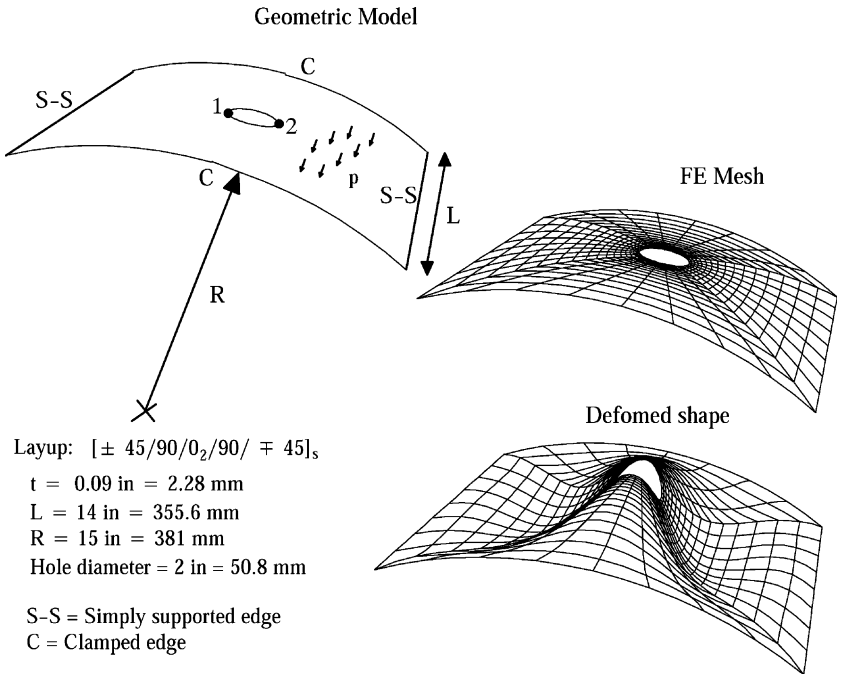

Fig. 18. Geometry and FE mesh for the laminated composite panel.

parameters were calibrated from short-term experiments up to 480 min, as shown in Table 5. In order to extend the range of analysis and examine the structural response for a long-term duration (1 year), a new Prony series was calibrated such that the rate of creep is fixed after 480 min. The Prony coefficients from the new calibrated series are listed in Table 8. The composite panel has $[\pm 45/90/0_2/\mp 45]_s$ layup. The geometry of this panel is taken from the post-buckling study performed by Knight and Starnes (1985). A uniform pressure is applied on the panel's top surface using a Heaviside step function. A static critical buckling pressure, p_{cr}, is first computed. A geometric imperfect mesh is constructed using the first five eigen modes and scaled by 1/20 of the panel's thickness. Fig. 18 also shows a typical deformed configuration. A relatively long-term creep response of the imperfect composite panel, under applied pressure of 0.8 and 0.9 p_{cr}, is shown in Fig. 19. An average radial displacement of the two points on the edge of the circular notch is

Table 8
Calibrated Prony series coefficients for the 5208 epoxy matrix

n	λ_n (s^{-1})	$D_n \times 10^{-5}$ MPa^{-1} (ksi^{-1})
1	1	7.77 (53.57)
2	10^{-1}	6.32 (43.58)
3	10^{-2}	3.60 (24.82)
4	10^{-3}	7.44 (51.30)
5	10^{-4}	3.95 (27.23)
6	10^{-5}	3.95 (27.23)
7	10^{-6}	4.96 (34.20)
8	10^{-7}	1.93 (13.31)

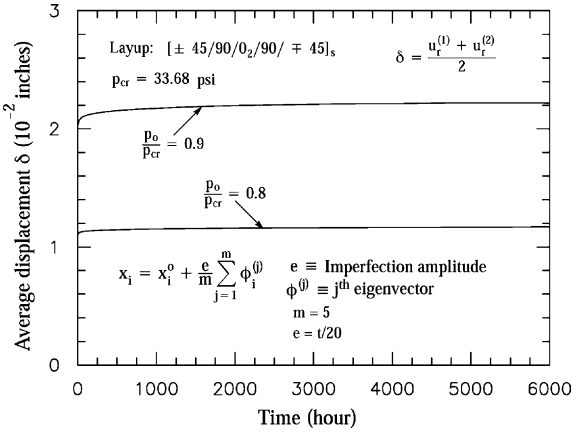

Fig. 19. Out-of plane creep displacement responses.

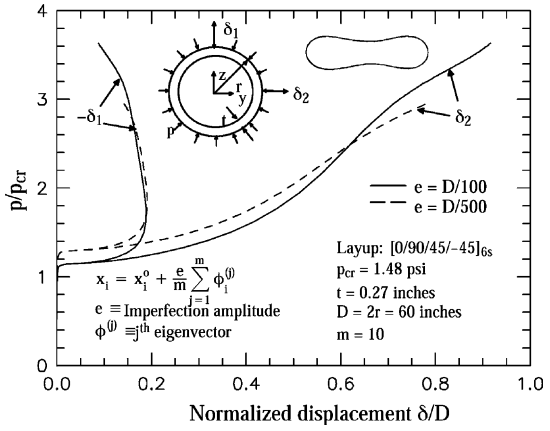

Fig. 20. Post-buckling responses of the laminated composite circular ring.

defined and used to quantify the creep response of the panel. The time-dependent response in this problem is not significantly nonlinear and viscoelastic buckling is not triggered.

The second structural application consists of a thick composite ring subjected to an external pressure. The ring is made of the same lamina as the previous example. The geometry and layup are shown in Fig. 20. The composite ring has outer radius of 30 in. and thickness of 0.27 in., with $[0/90/\pm 45]_{6s}$ layup. FE model with a quadratic shell typed element is then generated. A concentric external pressure is applied along the outer surface of the ring. Buckling analysis was first performed to obtain the critical load and the first ten eigen-modes used in the post-buckling analysis. The post-buckling response of the ring is shown in Fig. 20 for two different imperfection amplitudes, e: $D/100$ and $D/500$. A typical post-buckling deformation is also shown in Fig. 20. A stable post-buckling response is exhibited due to the positive stiffness that the structure retains in the post-buckling range. Long-term creep under different pressure levels: 0.8–3.1 p_{cr} are simulated with the initial imperfection $e = D/100$. Fig. 21(a)–(c) present the long-term creep response of the ring when

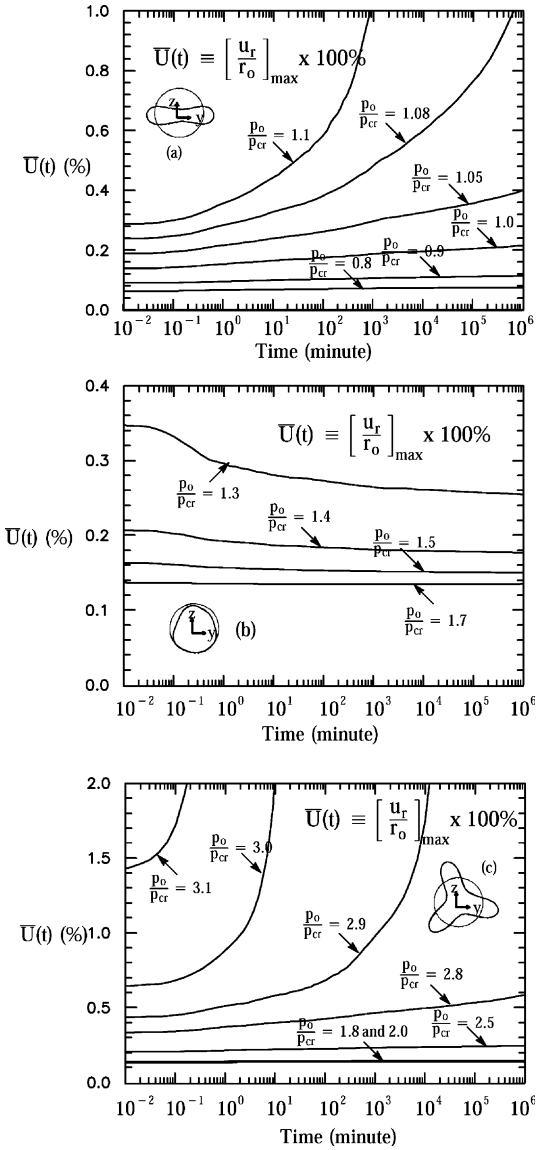

Fig. 21. Long-term creep response.

subjected to step pressure loads reported as a fraction of the critical buckling pressure. Loading ratios larger than one are also examined because of the positive residual stiffness of the ring after initial elastic buckling. The three figures are grouped according to the deformed shape. For $\frac{p}{p_{cr}} = 0.8$–1.1, the deformed shape follows the first mode and it is clear that viscoelastic buckling will ultimately occur for the cases where the loading ratio is greater than one. The second group of curves has loading ratio of $\frac{p}{p_{cr}} = 1.3$–1.7. The deformed shape in these cases is combined from both mode one and two. It is very interesting to note that while the applied load is greater than the buckling load, the likelihood of viscoelastic buckling has decreased perhaps due to the transition from mode-I to mode-II deformed configurations. Fig. 21(c) illustrates the curves for $\frac{p}{p_{cr}} = 1.8$–3.1. Nonlinear response and early viscoelastic buckling is easily observed.

6. Conclusion

A multi-scale micromechanical–structural viscoelastic analysis framework was examined. The nonlinear viscoelastic response for the matrix constituents can be calibrated from the overall creep response of off-axis laminated specimen. The material model was able to predict the multi-axial stress states that exist in different off-axis specimens that were not used for calibration. Modeling aging effects was also examined against experimental data available in the literature. The calibrated micromodel was successful in predicting the change in the elastic moduli due to aging and the effect of aging on creep. Finally, newly developed efficient numerical stress updates at the microlevel and for the Schapery nonlinear model were both used and implemented in a general purpose FE code to present a structural analysis modeling approach. Creep and viscoelastic buckling were examined using the analysis method.

Acknowledgements

This work was supported by NSF, through the Civil and Mechanical Systems (CMS) Division, and under grant number 9876080.

Appendix A

A numerical integration method for the Schapery nonlinear viscoelastic response of isotropic materials is described. An algorithm that is suitable for a displacement based FE material modeling environment with constant strain rate increments is proposed based on Haj-Ali and Muliana (2004).

The uniaxial transient compliance in Eq. (5) is expressed using a Prony series as

$$\Delta D^{\psi^t} = \sum_{n=1}^{N} D_n(1 - \exp[-\lambda_n \psi^t]) \tag{A.1}$$

where N is the number of terms, D_n is the nth coefficient of Prony series and λ_n is the nth reciprocal of the retardation time. Eq. (A.1) is then substituted for $\Delta J\psi$ and $\Delta B\psi$ in Eq. (6). Thus the deviatoric and volumetric strains are expressed as

$$e_{ij}^t = g_0^t J_0 S_{ij}^t + g_1^t g_2^t S_{ij}^t \sum_{n=1}^{N} J_n - g_1^t \sum_{n=1}^{N} J_n q_{ij,n}^t \tag{A.2}$$

$$q_{ij,n}^t = \int_0^t \exp[-\lambda_n(\psi^\tau - \psi^t)] \frac{\mathrm{d}g_2^\tau S_{ij}^\tau}{\mathrm{d}\tau} \mathrm{d}\tau \tag{A.3}$$

$$\varepsilon_{kk}^t = g_0^t B_0 \sigma_{kk}^t + g_1^t g_2^t \sigma_{kk}^t \sum_{n=1}^{N} B_n - g_1^t \sum_{n=1}^{N} B_n q_{kk,n}^t \tag{A.4}$$

$$q_{kk,n}^t = \int_0^t \exp[-\lambda_n(\psi^\tau - \psi^t)] \frac{\mathrm{d}g_2^\tau \sigma_{kk}^\tau}{\mathrm{d}\tau} \mathrm{d}\tau \tag{A.5}$$

A recursive integration forms for deviatoric and volumetric parts can be obtained from Eqs. (A.3) and (A.5) by dividing the integration into two parts. The first part includes the integral with limits $(0, t - \Delta t)$, i.e. up to the previous time step. The limits of the second part are taken as $(t - \Delta t, t)$, where t is the current time. The integration is carried by assuming a constant loading rate (linear function of $g_2^\tau \sigma^\tau$) over the current time

increment (Δt). Thus, the hereditary integral (Eqs. (A.3) and (A.5)) at the end of the current time t can be obtained from

$$q^t_{ij,n} = \exp[-\lambda_n \Delta\psi^t] q^{t-\Delta t}_{ij,n} + \left(g^t_2 S^t_{ij} - g^{t-\Delta t}_2 S^{t-\Delta t}_{ij}\right) \frac{1-\exp[-\lambda_n \Delta\psi^t]}{\lambda_n \Delta\psi^t} \tag{A.6}$$

$$q^t_{kk,n} = \exp[-\lambda_n \Delta\psi^t] q^{t-\Delta t}_{kk,n} + (g^t_2 \sigma^t_{kk} - g^{t-\Delta t}_2 \sigma^{t-\Delta t}_{kk}) \frac{1-\exp[-\lambda_n \Delta\psi^t]}{\lambda_n \Delta\psi^t} \tag{A.7}$$

where $q^{t-\Delta t}_{ij,n}$ and $q^{t-\Delta t}_{kk,n}$ terms in Eqs. (A.3) and (A.5) are the hereditary integral for every term in the Prony series at the end of previous time ($t - \Delta t$). A reduced time increment is defined by

$$\Delta\psi^t \equiv \psi^t - \psi^{t-\Delta t} \tag{A.8}$$

The total deviatoric and volumetric strains are formulated by substituting Eqs. (A.6) and (A.7) into Eqs. (A.2) and (A.4), respectively:

$$\begin{aligned} e^t_{ij} &= \frac{1}{2}\left[g^t_0 J_0 + g^t_1 g^t_2 \sum_{n=1}^{N} J_n - g^t_1 g^t_2 \sum_{n=1}^{N} J_n \frac{1-\exp[-\lambda_n \Delta\psi^t]}{\lambda_n \Delta\psi^t}\right] S^t_{ij} \\ &\quad - \frac{1}{2} g^t_1 \sum_{n=1}^{N} J_n \left[\exp[-\lambda_n \Delta\psi^t] q^{t-\Delta t}_{ij,n} - g^{t-\Delta t}_2 \frac{1-\exp[-\lambda_n \Delta\psi^t]}{\lambda_n \Delta\psi^t} S^{t-\Delta t}_{ij}\right] \\ &\equiv \overline{J}^t S^t_{ij} - \mathrm{d}^t_{ij} \end{aligned} \tag{A.9}$$

$$\begin{aligned} \varepsilon^t_{kk} &= \frac{1}{3}\left[g^t_0 B_0 + g^t_1 g^t_2 \sum_{n=1}^{N} B_n - g^t_1 g^t_2 \sum_{n=1}^{N} B_n \frac{1-\exp[-\lambda_n \Delta\psi^t]}{\lambda_n \Delta\psi^t}\right] \sigma^t_{kk} \\ &\quad - \frac{1}{3} g^t_1 \sum_{n=1}^{N} B_n \left[\exp[-\lambda_n \Delta\psi^t] q^{t-\Delta t}_{kk,n} - g^{t-\Delta t}_2 \frac{1-\exp[-\lambda_n \Delta\psi^t]}{\lambda_n \Delta\psi^t} \sigma^{t-\Delta t}_{kk}\right] \\ &\equiv \overline{B}^t \sigma^t_{kk} - V^t_{kk} \end{aligned} \tag{A.10}$$

The above equation allows for the incremental stress–strain calculation for a time increment Δt, which is then added to the total stress or strain from the previous time step ($t - \Delta t$). Eqs. (A.9) and (A.10) are used with some algebraic manipulations to derive the relations for the incremental deviatoric and volumetric strains. These are written as

$$\begin{aligned} \Delta e^t_{ij} &= e^t_{ij} - e^{t-\Delta t}_{ij} \\ &= \overline{J}^t S^t_{ij} - \overline{J}^{t-\Delta t} S^{t-\Delta t}_{ij} - \frac{1}{2}\sum_{n=1}^{N} J_n (g^t_1 \exp[-\lambda_n \Delta\psi^t] - g^{t-\Delta t}_1) q^{t-\Delta t}_{ij,n} \\ &\quad - \frac{1}{2} g^{t-\Delta t}_2 \sum_{n=1}^{N} J_n \left[g^{t-\Delta t}_1 \left(\frac{1-\exp[-\lambda_n \Delta\psi^{t-\Delta t}]}{\lambda_n \Delta\psi^{t-\Delta t}}\right) - g^t_1 \left(\frac{1-\exp[-\lambda_n \Delta\psi^t]}{\lambda_n \Delta\psi^t}\right)\right] S^{t-\Delta t}_{ij} \end{aligned} \tag{A.11}$$

$$\begin{aligned} \Delta\varepsilon^t_{kk} &= \varepsilon^t_{kk} - \varepsilon^{t-\Delta t}_{kk} \\ &= \overline{B}^t \sigma^t_{kk} - \overline{B}^{t-\Delta t} \sigma^{t-\Delta t}_{kk} - \frac{1}{3}\sum_{n=1}^{N} B_n (g^t_1 \exp[-\lambda_n \Delta\psi^t] - g^{t-\Delta t}_1) q^{t-\Delta t}_{kk,n} \\ &\quad - \frac{1}{3} g^{t-\Delta t}_2 \sum_{n=1}^{N} B_n \left[g^{t-\Delta t}_1 \left(\frac{1-\exp[-\lambda_n \Delta\psi^{t-\Delta t}]}{\lambda_n \Delta\psi^{t-\Delta t}}\right) - g^t_1 \left(\frac{1-\exp[-\lambda_n \Delta\psi^t]}{\lambda_n \Delta\psi^t}\right)\right] \sigma^{t-\Delta t}_{kk} \end{aligned} \tag{A.12}$$

Eqs. (A.11) and (A.12) are used to determine the unknown stress increment from a given strain increment and the previous history state, i.e. $q_{ij,n}^{t-\Delta t}$ and $q_{kk,n}^{t-\Delta t}$, $n = 1 \ldots N$. The problem is that the nonlinear stress functions at the current time (t) are not known. Therefore, an iterative method is needed in order to find the correct stress and its corresponding nonlinear viscoelastic parameters. An iterative scheme is developed by defining strain residuals. These residual equations can be defined by using either the incremental strains, Eqs. (A.11) and (A.12), or the total strains, Eqs. (A.9) and (A.10), respectively. The equations are combined to form the residual strain errors in the form:

$$
\begin{aligned}
R_{ij}^t &= \Delta e_{ij}^t + \frac{1}{3}\Delta\varepsilon_{kk}^t\delta_{ij} - \Delta\varepsilon_{ij}^t \\
&= \overline{J}^t\sigma_{ij}^t + \frac{1}{3}(\overline{B}^t - \overline{J}^t)\sigma_{kk}^t\delta_{ij} - \overline{J}^{t-\Delta t}\sigma_{ij}^{t-\Delta t} - \frac{1}{3}(\overline{B}^{t-\Delta t} - \overline{J}^{t-\Delta t})\sigma_{ij}^{t-\Delta t}\delta_{ij} \\
&\quad - \left\{ \frac{1}{2}\sum_{n=1}^{N} J_n(g_1^t \exp[-\lambda_n\Delta\psi^t] - g_1^{t-\Delta t})q_{ij,n}^{t-\Delta t} + \frac{1}{9}\left[\sum_{n=1}^{N} B_n(g_1^t \exp[-\lambda_n\Delta\psi^t] - g_1^{t-\Delta t})q_{kk,n}^{t-\Delta t}\right]\delta_{ij} \right. \\
&\quad + \frac{1}{2}g_2^{t-\Delta t}\sum_{n=1}^{N} J_n\left[g_1^{t-\Delta t}\left(\frac{1-\exp[-\lambda_n\Delta\psi^{t-\Delta t}]}{\lambda_n\Delta\psi^{t-\Delta t}}\right) - g_1^t\left(\frac{1-\exp[-\lambda_n\Delta\psi^t]}{\lambda_n\Delta\psi^t}\right)\right]S_{ij}^{t-\Delta t} \\
&\quad \left. + \frac{1}{9}g_2^{t-\Delta t}\sum_{n=1}^{N} B_n\left[g_1^{t-\Delta t}\left(\frac{1-\exp[-\lambda_n\Delta\psi^{t-\Delta t}]}{\lambda_n\Delta\psi^{t-\Delta t}}\right) - g_1^t\left(\frac{1-\exp[-\lambda_n\Delta\psi^t]}{\lambda_n\Delta\psi^t}\right)\right]\delta_{ij}\sigma_{kk}^{t-\Delta t} \right\} - \Delta\varepsilon_{ij}^t
\end{aligned}
\tag{A.13}
$$

A Jacobian matrix is formed by taking the derivative of the residual tensor with respect to the incremental stress as

$$
\begin{aligned}
\frac{\partial R_{ij}^t}{\partial\sigma_{kl}^t} &= \overline{J}^t\delta_{ik}\delta_{jl} + \frac{1}{3}(\overline{B}^t - \overline{J}^t)\delta_{ij}\delta_{kl} + \frac{\partial\Delta\overline{\sigma}^t}{\partial\sigma_{kl}^t}\left\{ \frac{\partial\overline{J}^t}{\partial\Delta\overline{\sigma}^t}\sigma_{ij}^t + \frac{1}{3}\left(\frac{\partial\overline{B}^t}{\partial\Delta\overline{\sigma}^t} - \frac{\partial\overline{J}^t}{\partial\Delta\overline{\sigma}^t}\right)\sigma_{kk}^t\delta_{ij} \right. \\
&\quad - \frac{1}{2}\frac{\partial g_1^t}{\partial\Delta\overline{\sigma}^t}\sum_{n=1}^{N} J_n\left[\exp[-\lambda_n\Delta\psi^t]q_{ij,n}^{t-\Delta t} - g_2^{t-\Delta t}\left(\frac{1-\exp[-\lambda_n\Delta\psi^t]}{\lambda_n\Delta\psi^t}\right)S_{ij}^{t-\Delta t}\right] \\
&\quad - \frac{1}{2}\frac{\partial a_\sigma^t}{\partial\Delta\overline{\sigma}^t}g_1^t\sum_{n=1}^{N} J_n\left[\exp[-\lambda_n\Delta\psi^t]\left(\frac{\lambda_n\Delta t q_{ij,n}^{t-\Delta t}}{a_\sigma^{t2}} + \frac{S_{ij}^{t-\Delta t}}{a_\sigma^t}\right) - g_2^{t-\Delta t}\left(\frac{1-\exp[-\lambda_n\Delta\psi^t]}{\lambda_n\Delta\psi^t}\right)S_{ij}^{t-\Delta t}\right] \\
&\quad - \frac{1}{9}\frac{\partial g_1^t}{\partial\Delta\overline{\sigma}^t}\sum_{n=1}^{N} B_n\left[\exp[-\lambda_n\Delta\psi^t]q_{kk,n}^{t-\Delta t} - g_2^{t-\Delta t}\left(\frac{1-\exp[-\lambda_n\Delta\psi^t]}{\lambda_n\Delta\psi^t}\right)\sigma_{kk}^{t-\Delta t}\right]\delta_{ij} \\
&\quad \left. - \frac{1}{9}\frac{\partial a_\sigma^t}{\partial\Delta\overline{\sigma}^t}g_1^t\sum_{n=1}^{N} B_n\left[\exp[-\lambda_n\Delta\psi^t]\left(\frac{\lambda_n\Delta t q_{kk,n}^{t-\Delta t}}{a_\sigma^{t2}} + \frac{\sigma_{kk}^{t-\Delta t}}{a_\sigma^t}\right) - g_2^{t-\Delta t}\left(\frac{1-\exp[-\lambda_n\Delta\psi^t]}{\lambda_n\Delta\psi^t}\right)\sigma_{kk}^{t-\Delta t}\right]\delta_{ij}\right\}
\end{aligned}
\tag{A.14}
$$

where

$$
\frac{\partial\Delta\overline{\sigma}^t}{\partial\sigma_{kl}^t} = \frac{3}{2}\frac{S_{ij}^t}{\Delta\overline{\sigma}^t}\left(\delta_{ij}\delta_{jl} - \frac{1}{3}\delta_{ij}\delta_{kl}\right)
$$

1. Input variables

$$\Delta\varepsilon_{ij}^{t},\ \Delta t \qquad \text{History}: \sigma_{ij}^{t-\Delta t},\ q_{ij,n}^{t-\Delta t},\ q_{kk,n}^{t-\Delta t}$$

2. Initialize linearized state

$$g_{\beta}^{t} = g_{\beta}^{t-\Delta t}\ ;\ \beta = 0,1,2 \qquad \Delta\psi^{t} = \Delta\psi^{t-\Delta t}$$

$$\mathbb{J}^{t,tr} = \mathbb{J}^{t}\left(g_{\beta}^{t},\ \Delta\psi^{t}\right) \qquad \mathbb{B}^{t,tr} = \mathbb{B}^{t}\left(g_{\beta}^{t},\ \Delta\psi^{t}\right)$$

$$\Delta\sigma_{ij}^{t,tr} = \Delta\sigma_{ij}^{t,tr}\left(\Delta S_{ij}^{t,tr},\ \Delta\sigma_{kk}^{t,tr}\right)$$

$$\sigma_{ij}^{t,(0)} = \sigma_{ij}^{t-\Delta t} + \Delta\sigma_{ij}^{t,tr}$$

3. Iterate for k=1, 2, 3 ....

3.1 Compute nonlinear parameters

$$g_{\beta}^{t,(k)} = 1 + \sum_{i=1}^{ng_{\beta}} \alpha_{i,\beta}\left\langle \frac{\bar{\sigma}^{(k)}}{\sigma_{o}} - 1 \right\rangle^{i}\ ;\ \beta = 0,1,2$$

$$a_{\sigma}^{t,(k)} = 1 + \sum_{i=1}^{na_{\sigma}} \delta_{i}\left\langle \frac{\bar{\sigma}^{(k)}}{\sigma_{o}} - 1 \right\rangle^{i}$$

3.2 Compute stress correction

$$\Delta\sigma_{ij}^{t,(k+1)} = \Delta\sigma_{ij}^{t,(k)} + \left[\frac{\partial R_{ij}^{t,(k)}}{\partial\Delta\sigma_{kl}}\right]^{-1} R_{kl}^{t,(k)}$$

$$\sigma_{ij}^{t,(k+1)} = \sigma_{ij}^{t,(k)} + \Delta\sigma_{ij}^{t,(k+1)}$$

3.1 Evaluate residual strain

$$R_{ij}^{t,(k)} = \Delta e_{ij}^{t,(k)} + \frac{1}{3}\delta_{ij}\Delta\varepsilon_{kk}^{t,(k)} - \Delta\varepsilon_{ij}^{t}$$

IF $\| R^{t,(k)} \| \le \text{Tol}$ THEN GOTO 4 and EXIT

ENDIF GOTO 3

4. Update stress, consistent tangent stiffness, and history variables

$$\sigma_{ij}^{t} \leftarrow \sigma_{ij}^{t,(k+1)} \qquad C_{ij}^{t} \leftarrow \left[\frac{\partial R_{ij}^{t,(k)}}{\partial\Delta\sigma_{kl}}\right]^{-1} \qquad q_{ij,n}^{t} \leftarrow q_{ij,n}^{t,(k+1)} \qquad q_{kk,n}^{t} \leftarrow q_{kk,n}^{t,(k+1)}$$

Fig. 22. Recursive–iterative algorithm for nonlinear isotropic viscoelastic model.

The complete numerical algorithm, which is used to provide the correct stress and its corresponding nonlinear parameters for a given strain increment, is explained in Fig. 22.

Appendix B

The following equation is the detailed general form of the $\overline{A}_{ba}$ matrix of order (11×13) derived in the micromodel for the unidirectional composite in Eq. (28):

$$\overline{A}_{ba} = \begin{bmatrix}
-C_{12}^{(1)} & C_{12}^{(2)} & 0 & 0 & -C_{22}^{(1)} & 0 & 0 & 0 & -C_{23}^{(1)} & C_{23}^{(2)} & 0 & C_{25}^{(2)} & 0 \\
0 & 0 & -C_{12}^{(3)} & C_{12}^{(4)} & 0 & C_{22}^{(3)} & 0 & -C_{24}^{(3)} & 0 & 0 & 0 & 0 & 0 \\
0 & C_{14}^{(2)} & 0 & 0 & 0 & 0 & -C_{44}^{(1)} & 0 & 0 & C_{34}^{(2)} & 0 & C_{45}^{(2)} & 0 \\
0 & 0 & -C_{14}^{(3)} & C_{14}^{(4)} & 0 & -C_{24}^{(3)} & 0 & -C_{44}^{(3)} & 0 & 0 & 0 & 0 & 0 \\
-C_{12}^{(1)} & 0 & C_{13}^{(3)} & 0 & -C_{23}^{(1)} & C_{23}^{(3)} & 0 & C_{34}^{(3)} & -C_{22}^{(1)} & 0 & 0 & 0 & 0 \\
0 & -C_{13}^{(2)} & 0 & C_{13}^{(4)} & 0 & 0 & 0 & 0 & 0 & -C_{33}^{(2)} & 0 & -C_{35}^{(2)} & 0 \\
0 & 0 & C_{15}^{(3)} & 0 & 0 & C_{25}^{(3)} & 0 & C_{45}^{(3)} & 0 & 0 & -C_{44}^{(1)} & 0 & 0 \\
0 & -C_{15}^{(2)} & 0 & C_{15}^{(4)} & 0 & 0 & 0 & 0 & 0 & -C_{35}^{(2)} & 0 & -C_{55}^{(2)} & 0 \\
0 & C_{16}^{(2)} & 0 & 0 & 0 & 0 & 0 & 0 & 0 & C_{36}^{(2)} & 0 & C_{56}^{(2)} & -C_{66}^{(1)} \\
0 & 0 & C_{16}^{(4)} & 0 & 0 & C_{26}^{(3)} & 0 & C_{46}^{(3)} & 0 & 0 & 0 & 0 & -C_{66}^{(1)} \\
0 & -C_{16}^{(2)} & 0 & C_{16}^{(4)} & 0 & 0 & 0 & 0 & 0 & -C_{36}^{(2)} & 0 & -C_{56}^{(2)} & 0
\end{bmatrix} \tag{B.1}$$

The $\overline{A}_{bb}$ general form in the order of (11×11) in the micromechanical derivation in Eq. (28) is

$$\overline{A}_{bb} = \begin{bmatrix}
C_{22}^{(2)} & 0 & C_{24}^{(2)} & 0 & 0 & 0 & 0 & 0 & C_{26}^{(2)} & 0 & 0 \\
0 & C_{22}^{(4)} & 0 & C_{24}^{(4)} & -C_{23}^{(3)} & C_{23}^{(4)} & -C_{25}^{(3)} & C_{25}^{(4)} & 0 & -C_{26}^{(3)} & C_{26}^{(4)} \\
C_{24}^{(2)} & 0 & C_{44}^{(2)} & 0 & 0 & 0 & 0 & 0 & C_{46}^{(2)} & 0 & 0 \\
0 & C_{24}^{(2)} & 0 & C_{44}^{(4)} & -C_{34}^{(3)} & C_{34}^{(4)} & -C_{45}^{(3)} & C_{45}^{(4)} & 0 & -C_{46}^{(3)} & C_{46}^{(4)} \\
0 & 0 & 0 & 0 & C_{33}^{(3)} & 0 & C_{35}^{(3)} & 0 & 0 & C_{36}^{(3)} & 0 \\
-C_{23}^{(2)} & C_{23}^{(4)} & -C_{34}^{(2)} & C_{34}^{(2)} & 0 & C_{33}^{(4)} & 0 & C_{35}^{(4)} & -C_{36}^{(2)} & 0 & C_{36}^{(4)} \\
0 & 0 & 0 & 0 & C_{35}^{(3)} & 0 & C_{55}^{(3)} & 0 & 0 & C_{56}^{(3)} & 0 \\
-C_{25}^{(2)} & C_{25}^{(4)} & -C_{45}^{(2)} & C_{45}^{(4)} & 0 & C_{35}^{(4)} & 0 & C_{55}^{(4)} & -C_{56}^{(2)} & 0 & C_{56}^{(4)} \\
C_{26}^{(2)} & 0 & 0 & 0 & 0 & 0 & 0 & 0 & C_{66}^{(2)} & 0 & 0 \\
0 & 0 & 0 & 0 & C_{36}^{(3)} & 0 & C_{56}^{(3)} & 0 & 0 & C_{66}^{(3)} & 0 \\
-C_{26}^{(2)} & C_{26}^{(4)} & -C_{46}^{(2)} & C_{46}^{(4)} & 0 & C_{36}^{(4)} & 0 & C_{56}^{(4)} & -C_{66}^{(2)} & 0 & C_{66}^{(4)}
\end{bmatrix} \tag{B.2}$$

References

ABAQUS, Hibbitt, Karlsson and Sorensen, Inc., User's Manual, Version 6.3, 2002.

Aboudi, J., 1990. Micromechanical characterization of the non-linear viscoelastic behavior of resin matrix composites. Composites Science and Technology 38, 371–386.

Aboudi, J., 1991. Mechanics of Composite Materials: A Unified Micromechanical Approach. Elsevier.

Barbero, E.J., Luciano, R., 1995. Micromechanical formulas for the relaxation tensor of linear viscoelastic composites with transversely isotropic fibers. International Journal of Solids and Structures 32 (13), 1859–1872.

Bradshaw, R.D., Brinson, L.C., 1999a. A continuous test data method to determine a reference curve and shift rate for isothermal physial aging. Polymer Engineering and Science 39 (2), 211–235.

Bradshaw, R.D., Brinson, L.C., 1999b. Mechanical response of linear viscoelastic composite laminates incorporating non-isothermal physical aging effects. Composite Science and Technology 59, 1411–1427.

Brinson, L.C., Gates, T.S., 1995. Effects of physical aging on long term creep of polymers and polymer matrix composites. International Journal of Solids and Structures 32, 827–846.

Fisher, F.T., Brinson, L.C., 2001. Viscoelastic interphases in polymer–matrix composites: theoretical models and finite element analysis. Composites Science and Technology 61 (January), 731–748.

Gates, T.S., Veazie, D.R., Brinson, L.C., 1997. Creep and physical aging in a polymeric composite: comparison of tension and compression. Journal of Composite Materials 31 (24), 2478–2505.

Haj-Ali, R.M., Muliana, A.H., 2003. Micromechanical constitutive framework for the nonlinear viscoelastic behavior of pultruded composite materials. International Journal of Solids Structures 40, 1037–1057.

Haj-Ali, R.M., Muliana, A.H., 2004. Numerical finite element formulation of the schapery nonlinear viscoelastic material model. International Journal of Numerical Methods and Engineering 59 (1), 25–45.

Haj-Ali, R.M., Pecknold, D.A., Ahmad, F., 1993. Integrated micromechanical and structural finite element analysis of laminated composites. The 1993 ABAQUS users conference, June, Achen, Germany, pp. 233–247.

Hiel, C.C., Brinson, H.F., Cardon, A.H., 1983. The nonlinear viscoelastic response of resin matrix composites. In: Marshall, I.H. (Ed.), Composite Structures, vol. 2, Applied Science, pp. 271–281.

Hu, H., Sun, C.T., 2000. The characterization of physical aging in polymeric composites. Composites Science and Technology 60, 2693–2698.

Knight Jr., N.F., Starnes Jr., J.H., 1985. Postbuckling behavior of axially compressed graphite–epoxy cylindrical panels with circular holes. ASME Journal of Pressure Vessels Technology 107, 394–402.

Lou, Y.C., Schapery, R.A., 1971. Viscoelastic characterization of a nonlinear fiber-reinforced plastic. Journal of Composite Materials 5 (April), 208–234.

Pasricha, A., Dillard, D.A., Tuttle, M.E., 1997. Effect of physical aging and variable stress history on the strain response of polymeric composites. Composite Science and Technology 57, 1271–1279.

Pecknold, D.A., Haj-Ali, R.M., 1993. Integrated micromechanical/structural analysis of laminated composites. In: Hyer, M.W. (Ed.), Mechanics of Composite Materials—Nonlinear Effects, AMD-vol. 159, Proceedings of the 1st Joint Mechanics Meeting of SES/ASME/ASCE, June, Charlottesville, VA, pp. 197–206.

Sadkin, Y., Aboudi, J., 1989. Viscoelastic behavior of thermo-rheologically complex resin matrix composites. Composites Science and Technology 36, 351–365.

Schaffer, B.G., Adams, D.F., 1981. Nonlinear viscoelastic analysis of a unidirectional composite material. Journal of Applied Mechanics 48 (December), 859.

Schapery, R.A., 1969. On the characterization of nonlinear viscoelastic materials. Polymer Engineering and Science 9 (4), 295–310.

Struik, L.C.E., 1978. Physical Aging In Amorphous Polymers and Other Materials. Elsevier Scientific Publishing Company, New York.

Tuttle, M.E., Brinson, H.F., 1986. Prediction of the long-term creep compliance of general composite laminates. Experimental Mechanics (March), 89–102.

Yancey, R.N., Pindera, M.J., 1990. Micromechanical analysis of the creep response of unidirectional composites. Journal of Engineering Material and Technology 112 (April), 157–163.

Yeow, Y.T., Morris, D.H., Brinson, H.F., 1979. Time–temperature behavior of a unidirectional graphite/epoxy composite. In: Tsai, (Ed.), Composite Material Testing and Design (Fifth Conference), ASTM STP 674. ASTM, pp. 263–281.